Investigating hard Fermi sources with H.E.S.S.

Masterarbeit aus der Physik

Vorgelegt von
Jens Holzmeier

19. Dezember 2016

Lehrstuhl für Physik
Naturwissenschaftliche Fakultät
Friedrich-Alexander-Universität Erlangen-Nürnberg

1. Gutachter: Prof. Dr. Stefan Funk
2. Gutachter: Prof. Dr. Christopher van Eldik

Abstract

The aim of this thesis was to investigate sources of a pre-release version of the upcoming Fermi 3FHL catalog with the H.E.S.S. instrument. To this purpose, a software tool to calculate H.E.S.S. sensitivities for any given position in the sky using already available data or a set of input parameters was developed. The produced sensitivity curves agree with results from the HAP software, which were used as a verification.

The subsequent analysis of the 3FHL sources focused on galactic sources. In total 56 sources were deemed as being observable with H.E.S.S. above 1 TeV within 30 h. Five of them were selected for further investigation as they provided the highest and most constant flux. This revealed that due to their extensions only four are actually expected to be seen with the available data. However, the produced significance maps showed no excess at any of the target positions. A likely reason are cutoffs in the spectra not observed by Fermi. The calculated upper limits for the sources were in good agreement with the calculated sensitivities as well as the Fermi spectra. Suggesting further H.E.S.S. observations for these positions seems inappropriate as more than 30 h of data are already available for most of the sources.

Besides, for 22 of the remaining sources H.E.S.S. data was available. Analyzing them produced the same results. However, as some of these source have less than 15 h of data, they may be interesting for follow-up observations.

Kurzfassung

Das Ziel dieser Arbeit war die Untersuchung von Fermi Quellen mit H.E.S.S. anhand einer vorab veröffentlichten Version des anstehenden 3FHL Katalogs. Zu diesem Zweck wurde eine Software entwickelt, welche die H.E.S.S. Sensitivität für eine beliebige Himmelsposition basierend auf schon erfassten Daten oder einer Reihe an Eingangsparametern berechnet. Die produzierten Sensitivitäten stimmen mit den Resultaten der HAP Software überein, die zur Verifikation verwendet wurde.

Die Analyse der 3FHL Quellen konzentrierte sich auf galaktische Quellen. Insgesamt wurden 56 Quellen gefunden, die überhalb von 1 TeV und innerhalb von 30 h mit H.E.S.S. als beobachtbar eingestuft wurden. Fünf dieser Quellen wurden näher untersucht, da sie den höchsten und konstantesten Fluss aufgewiesen haben. Dabei kam heraus, dass aufgrund ihrer Ausdehnung nur vier tatsächlich detektierbar sein sollten. Die erstellten Signifikanzkarten offenbarten jedoch für keine der Quellen ein Signal. Ein wahrscheinlicher Grund hierfür ist die Möglichkeit, dass die Spektren der Quellen Cutoffs aufweisen, die Fermi nicht detektiert hat. Die errechneten Upper Limits stimmten sowohl mit den errechneten Sensitivitäten, als auch mit den Fermi Spektren der Quellen gut überein. Da die meisten Quellen schon über 30 h an Daten haben, erscheint es unangebracht weitere Beobachtungen vorzuschlagen.

Für 22 der restlichen Quellen waren ebenfalls H.E.S.S. Daten verfügbar. Eine Analyse dieser brachte die gleichen Ergebnisse hervor. Da allerdings einige dieser Objekte weniger als 15 h an Daten haben, könnten einige von ihnen interessant genug für Follow-Up Studien sein.

Contents

1. Introduction

Astronomy is one of the oldest natural sciences. Even the early civilizations in recorded history observed the night sky. They often identified celestial objects with gods and spirits and related certain phenomena such as rain, drought, the seasons or tides to them. But they also observed the constellations and motions of stars and planets. This enabled them to navigate over longer distances or set calenders, which were important to agricultural societies, in which the harvest depended on planting at the correct time of the year.

The early stages of astronomical observations were done with the naked eye and thus were very limited. The invention of the telescope and its successive development allowed scientists to expand their knowledge by observing even fainter objects. Today observations are no longer limited to optical light, but are possible in all ranges of the electromagnetic spectrum. Studies in these regions are crucial as they provide many additional information on the physics of sources and the universe itself.

The most energetic photons in the electromagnetic spectrum are the ones relevant for this master thesis and come from γ-rays having energies up to 10^{12} eV. As even the hottest known objects in the universe can not produce such energies, thermal processes must be ruled out as a possible origin. A solution to this problem is the production through emitted electrons and protons which are able to produce γ-rays through secondary mechanisms.

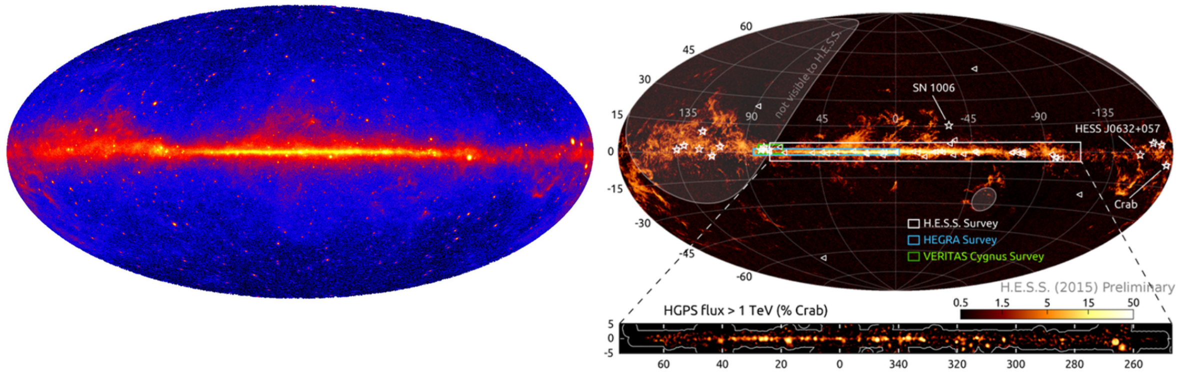

Figure 1.1.: **Left:** All-sky map at energies above 1 GeV based on five years of data from the Fermi-LAT instrument. [1] **Right:** Planck CO all-sky map with the H.E.S.S. Galactic Plane Survey (HGPS) region illustrated as well as a flux map (below). Fermi-LAT identified galactic 1FHL sources (triangles) and known galactic TeV sources (white stars) outside the HGPS region have been marked. The HEGRA Galactic Plane Survey and VERITAS Cygnus survey regions are also illustrated. [2]

The detection of γ-rays on Earth is difficult as our atmosphere blocks them. To circumvent this problem two approaches are possible: launching instruments into orbit like the Fermi satellite or using ground-based Imaging Air Cherenkov Telescopes (IACT) like the H.E.S.S. array in Namibia. The latter are utilizing an indirect detection mechanism through the Cherenkov light emitted by air showers in the atmosphere which are triggered by primary γ-ray photons.

The aim of this master thesis was the investigation of hard γ-ray sources from the Fermi-LAT (Large Area Telescope) with the H.E.S.S. instrument. The Fermi-LAT operates in the energy range of 20 MeV up to 2 TeV and monitors the entire sky with its big field of view (see Figure 1.1). IACTs like H.E.S.S. have much smaller field of views but are able to observe γ-rays up to tens of TeV because of their bigger detection area. Both instruments complement each other in these regards. The motivation behind this work therefore was to find Fermi sources that are suitable for H.E.S.S. follow-up observation. This way H.E.S.S. would be able to extend the energy range of the collected data and help connecting the GeV and TeV data. To decide which sources are suitable candidates for follow-up observations a sensitivity tool was developed. It is able to provide H.E.S.S. sensitivity curves for any sky position based on either already available data or a set of specified parameters. The tool was then put to use by investigating sources from a pre-release version of the 3FHL catalog.
This master thesis is organized as follows: Chapter 2 describes all essential and relevant principles of γ-ray astronomy. This includes the topic of cosmic radiation and its production mechanisms as well as the fundamentals of IACTs and the H.E.S.S. telescope array. In Chapter 3 the developed sensitivity tool is covered. Aspects like the estimation of γ-events along with the implementation of a background model and extracting the right data from it are explained. This rounds off with several verification steps for interim results and the final sensitivity curves. Chapter 4 deals with the analysis of the 3FHL sources. It begins with explaining how the analysis was performed and discusses the outcomes from it in the end. Finally, Chapter 5 briefly sums up the overall results of this thesis and gives some outlook of the next steps that could be taken.

2. γ-Astronomy

This chapter introduces the fundamental principles and topics of γ-astronomy which are relevant to this thesis. It starts by introducing cosmic rays and cosmic γ-rays and highlighting the differences between the two. As the name title of the chapter already suggests, the focus of interest lies in the cosmic γ-radiation. Therefore the mechanisms for the origin of γ-rays are explained along with some possible sources. Afterwards the detection principles for ground-based telescopes are presented, the term "sensitivity" is defined and the H.E.S.S. experiment is introduced.

2.1. Cosmic Radiation and Cosmic γ-Radiation

The field of cosmic ray physics started with its discovery by Victor Hess in 1912. Up until then it was generally believed that the ionization of the air was caused only by radiation of radioactive materials on the ground. In 1912 Hess carried electrometers up to altitudes of 5300 m in a balloon and measured the ionization rate. He found that ionization levels increased with increasing altitude. He measured the same behavior while performing flights during nighttime and even one during a near total solar eclipse, which made him rule out the Sun as a possible source. Hess concluded that his observations *"are best explained by the assumption that a radiation of very great penetrating power enters our atmosphere from above"* [3]. In 1936 the Nobel Prize in Physics was awarded to him for his discovery.

The term "radiation" is still used today even though we now know that cosmic radiation consist of charged particles. About 89 % are protons (hydrogen nuclei), 9 % are α-particles (helium nuclei) and 1 % are heavier nuclei. The energy spectrum of cosmic radiation extends up to energies of 10^{20} eV and is described by a power law

$$\frac{dN}{dE} \propto E^{-\gamma} \tag{2.1}$$

with a spectral index of $\gamma \simeq 2.7$ (see Figure 2.1). It also contains some distinct features like the so-called *knee* at 10^{16} eV and the *ankle* at 10^{19} eV. At the knee the spectral index γ changes from 2.7 to 3.1 whereas at the ankle the index changes back to 2.7. Cosmic rays below the knee are thought to be produced within the galaxy (e.g. in supernova remnants) while one assumes an extragalactic origin (AGNs, blazars, etc.) at energies above the ankle. The reason for the transition is the limited strength of the galactic magnetic field which becomes incapable of containing higher energy particles within it.

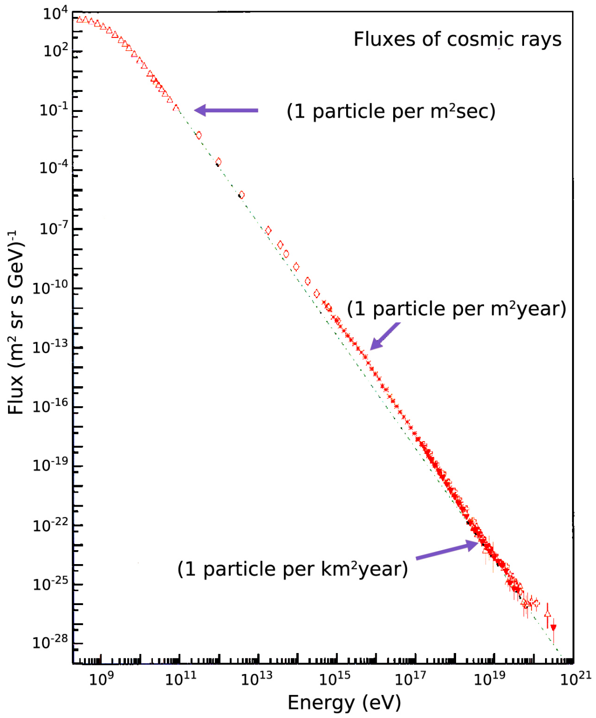

Figure 2.1.: Cosmic ray spectrum [4]

2.1.1. Possible Sources of Cosmic Rays

The study of cosmic rays is a very active field in science for over a century now, but their exact origin is still not absolutely clear. There is however strong evidence that supernova remnants (SNRs) are sources of cosmic rays [5–8]. Recent studies have also suggested the Galactic Center as a possible origin [9]. The problem, which makes finding sources complicated, is the charge of the particles. Due to galactic and extragalactic magnetic fields cosmic rays are deflected on their way from the source to the observer, which makes reconstructing their original direction impossible. A way to avoid this problem is to instead observe (very high energy) cosmic γ-rays.

It is generally assumed that the galactic cosmic rays below the knee are produced by a single mechanism or class of sources. Supernova remnants (SNRs) are a favored source for galactic cosmic rays. One reason for this is that a theoretical well established acceleration mechanism at SNR shock fronts already exists, called *diffuse first order Fermi shock acceleration*[1]. Another reason is that supernovae and the resulting SNRs are the only known possible sources to provide enough energy [10].

Above the knee in the cosmic ray spectrum both galactic and extragalactic sources have been suggested. Generally compact objects with jets such as quasars or active galactic nuclei (AGNs) seem plausible.

---

[1] A detailed description of first order Fermi shock acceleration can be found in Blandford & Eichler (1987) or Malkov & Drury (2001).

2.1.2. Production Mechanisms of γ-Rays

γ-rays are produced by the interaction of cosmic rays with interstellar material or radiation fields. One can differentiate between three different production mechanisms: leptonic emission, hadronic emission and annihilation of dark matter. Each process has different characteristic features that can help identify the underlying production mechanism once the γ-rays are observed.

Leptonic Emission

There are three underlying processes that fall in the category of leptonic emission: synchrotron radiation, inverse Compton scattering and bremsstrahlung.
Synchrotron radiation is emitted when relativistic charged particles are forced to travel in a curved path by a magnetic field B. For an electron with an initial energy E_e the energy E_{sync} of the emitted photon is described by [11]

$$E_{sync} = 0.2 \frac{B}{10\,\mu\mathrm{G}} \left(\frac{E_e}{1\,\mathrm{TeV}} \right)^2 \mathrm{eV} \tag{2.2}$$

This assumes a mono-energetic population of electrons and isotropic distribution of pitch angles. The spectral shape of the synchrotron spectrum shows a peak with a tail to higher energies. Looking at a TeV electron in a typical 10 μG magnetic field the distribution peaks at 0.2 eV. However, a more realistic approach uses an energy distribution for the electrons that follows a power law with index α_e. Consequently, the differential synchrotron spectrum then also follows a power law. Its spectral index is $\Gamma_{sync} = \frac{\alpha_e + 1}{2}$ (see Figure 2.2).

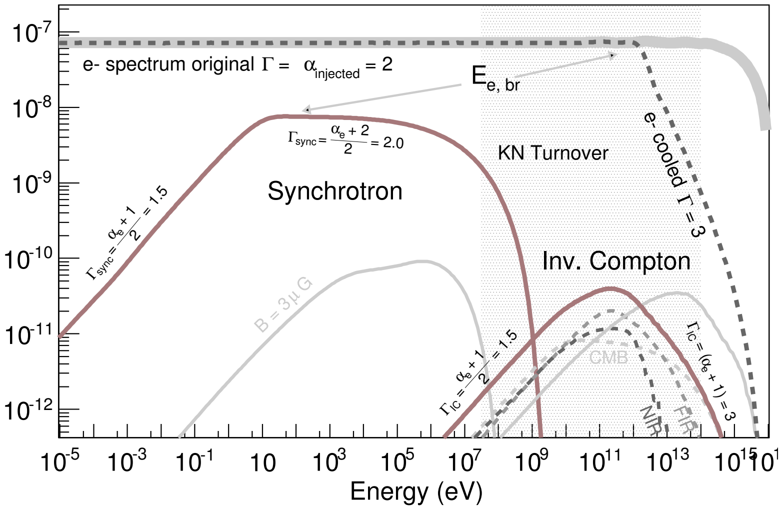

Figure 2.2.: Spectral energy distribution of γ-rays due to leptonic emission (electrons). The shaded gray region shows the sensitive range of current γ-ray detectors. [11]

Inverse Compton scattering describes the effect of relativistic electrons and positrons up-scattering present low energy photons (e.g. found in the cosmic microwave background) to very high energies. This produces a broad spectral distribution of high-energy photons. Again, assuming mono-energetic electrons scatter on target photons, the peak of the distribution is described by

$$E_{IV} = 5 \times 10^9 \frac{E_{ph}}{10^{-3}\,\mathrm{eV}} \left(\frac{E_e}{1\,\mathrm{TeV}} \right)^2 \mathrm{eV} \tag{2.3}$$

The similarities between Equation 2.2 and 2.3 lead to the fact that both synchrotron and inverse Compton spectra have the same overall shape, though at different energies. Both spectra, when assuming an electron distribution of $dN/dE \propto E^{\alpha_e}$, will have a slope of $\Gamma = \frac{\alpha_e+1}{2}$. However, at higher energies the turnover in the inverse Compton spectrum will be much steeper with an index of $\Gamma = \alpha_e + 1$.

A third possible production mechanism is bremsstrahlung. Cosmic ray electrons, that are emitted by pulsars for example, emit γ-rays when they strike gas or dust in their nearby medium and are being decelerated.

Hadronic Emission

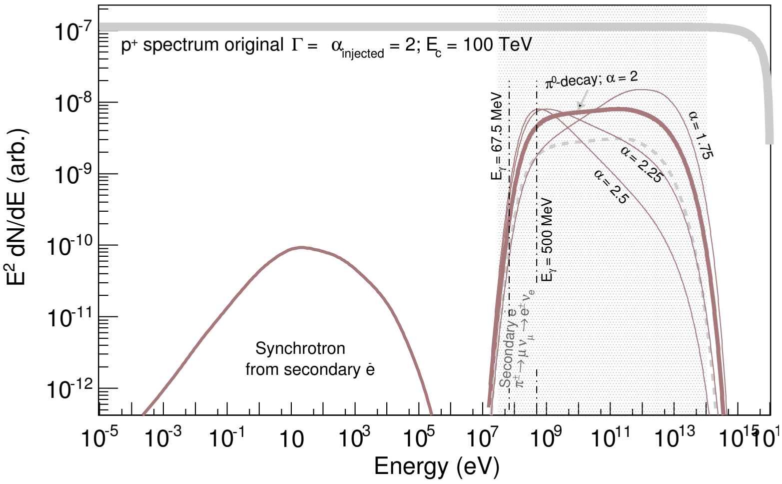

Figure 2.3.: Spectral energy distribution of accelerated protons and γ-rays resulting from inelastic collisions with interstellar material. The shaded gray region shows the sensitive range of current γ-ray detectors. [11]

Another production mechanism for γ-rays is the interaction of high-energy protons with interstellar material (e.g. gas clouds) during which neutral pions π^0 are created. A possible interaction chain is

$$p + p \rightarrow \pi^0 + X$$

The π^0 particle has a very short lifetime (8.4×10^{-17} s) and decays in two photons (γ-rays) 98.8 % of the time.

$$\pi^0 \rightarrow \gamma + \gamma$$

The resulting γ-rays range from a few MeV up to about 10 % of the energy of the primary proton [12]. A 1 PeV proton would therefore result in a 100 TeV photon.
Figure 2.3 also shows the synchrotron spectrum form secondary electrons resulting from inelastic pp-interactions via the decay chains of charged pions $\pi^{\pm} \rightarrow \mu + \nu_{\mu} \rightarrow e^{\pm}\nu_{e}$. Their energies lie below the typical sensitive range of current γ-ray detectors (shaded grey area).

Dark Matter Annihilation

The third possible component adding to the flux of γ-rays is dark matter annihilation. Dark matter is an undefined type of matter in the Universe and dominates its mass density. It is also the driving force in structure formation. There are several different models describing what dark matter could be made of, but the favored candidate (so far) are weakly interacting massive particles (WIMPs). These are non-relativistic particles with masses in the GeV range and only interacting through gravity or the weak force. They are also expected to mutually annihilate under the emission of γ-rays. The resulting products can be different and depend strongly on the annihilation channel. Supersymmetry typically predicts the annihilation of the lightest particle (e.g. the neutralino) into $b\overline{b}$, $t\overline{t}$, $\tau^{+}\tau^{-}$, $W^{+}W^{-}$ or ZZ. Unfortunately all of these channels are ultimately dominated by the previously discussed leptonic emission (see Figure 2.4).

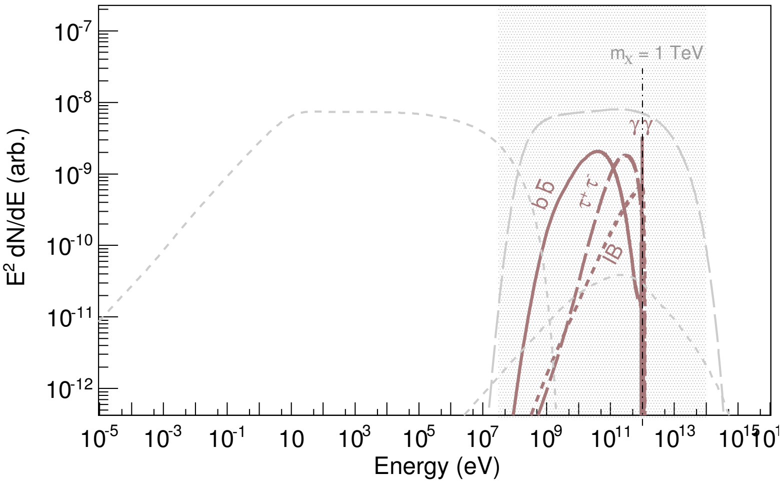

Figure 2.4.: Spectral energy distribution of γ-rays resulting from neutralino annihilation. The spectra from the leptonic and hadronic emission are shown in light gray dashed lines. The shaded gray region shows the sensitive range of current γ-ray detectors. [11]

2.2. γ-Ray Detection

Earth's atmosphere completely blocks cosmic γ-radiation, as well as other wavelengths (see Figure 2.5). One way to avoid this problem is the use of space-based detectors like the Fermi-LAT. Another possible solution is the detection via ground-based Imaging Atmospheric Cherenkov Telescopes (IACTs). They detect the Cherenkov light emitted by particle showers which are triggered when cosmic particles hit the top layers of Earth's atmosphere. An advantage of ground-based experiments is the ability to detect γ-rays in the TeV range. As they are much less limited in size compared to space-based instruments, larger detection areas are possible to achieve.
The underlying physics of γ-ray detection with IACTs shall be explained in the following chapters.

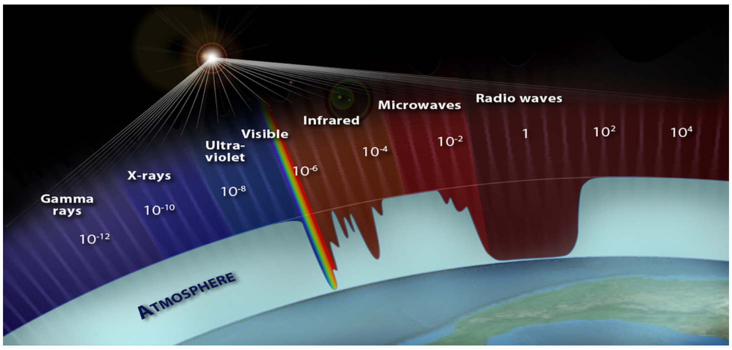

Figure 2.5.: Atmospheric transmissivity for different wavelengths [13]

2.2.1. Atmospheric Particle Showers

When energetic cosmic particles hit the top of Earth's atmosphere, they interact with the air molecules and create secondary particles. If the primary particle has a high enough energy, the secondary particles can interact and create further particles. This interaction chain continues until the energy drops below a critical value. That way an air shower is created. The type and properties of air showers depend strongly on the energy and type of the primary particle (see Figure 2.6).
The following three underlying interaction mechanisms play an important part in creating such air showers:

> **Bremsstrahlung:** When a charged particle (e.g. an electron) is decelerated in the Coulomb field of another charged particle (e.g. an atomic nucleus), it emits a photon. The energy of the photon corresponds to the energy loss of the particle. It effects mainly light particles since the energy loss is inversely proportional to the particle's mass.

Pair production: An incoming photon can create a particle-antiparticle pair if its energy is higher than the combined rest mass of the particle pair ($E_\gamma \geq 1.022\,\mathrm{MeV}$ in case of electron-positron production). The photon also has to be in the Coulomb field of an atomic nucleus in order to satisfy conservation of momentum.

Strong interactions: If a hadron (e.g. a proton) enters the atmosphere, it scatters on other nuclei via the strong nuclear force and further secondary hadrons and leptons are created.

Depending on the incoming primary particle different interaction mechanism are involved in the development of atmospheric particle showers. Generally one distinguishes between two types of particle showers: electromagnetic showers and hadronic showers.

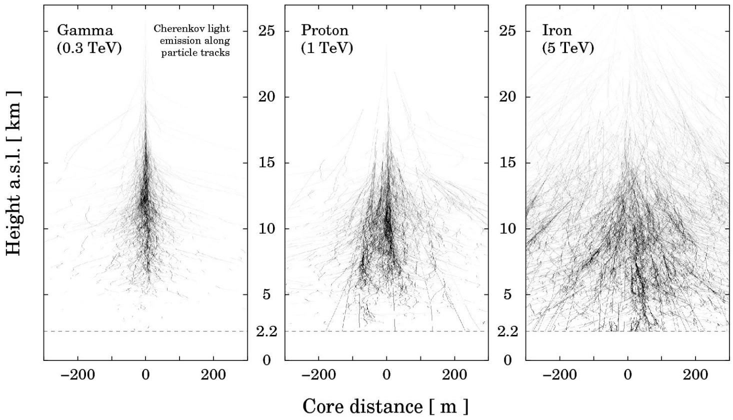

Figure 2.6.: Simulation of Cherenkov light production for different primary particles. The darkness of the particle tracks indicate the amount of emission. [14]

Electromagnetic Showers

When a γ-photon with the energy E_0 enters Earth's atmosphere, it interacts with an air molecule and produces an electron-positron pair. The electron and positron then emit further photons through bremsstrahlung which again are able to create more particles through pair production. This chain of interaction continues until the particles' energy drop below a critical value E_c ($E_c = 83\,\mathrm{MeV}$ for air). At that point ionization becomes the dominant process and thus no more new particles are created (see Figure 2.7). Because pair-production and bremsstrahlung are both electromagnetic processes, this shower type is called an electromagnetic air shower.

This simplified and schematic description of the development of electromagnetic showers was initially proposed by Heitler [15]. Besides the assumption that only pair-production and bremsstahlung are considered (whereas ionization is neglected), it also assumes that the energy of the incoming photon is equally divided between the positron and electron after the pair-production. Furthermore, both particles emit photons after exactly one radia-

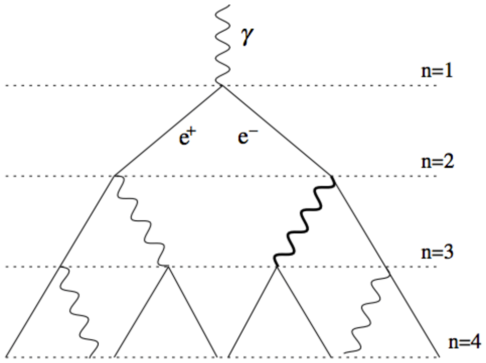

Figure 2.7.: Simplified and schematic model of the development of electromagnetic showers according to Heitler. [16]

tion length X_0. The radiation length is defined by the following function and describes the amount of traversed matter after which an electron loses a significant fraction of its energy by bremsstrahlung [17]:

$$X_0 = \left[4\alpha r_e^2 \frac{N_A}{A} Z^2 \ln(183\, Z^{-\frac{1}{3}})\right]^{-1} \left[\mathrm{g\,cm^{-2}}\right] \tag{2.4}$$

where $\alpha = \frac{1}{137}$ is the fine-structure constant, r_e the radius of the electron, N_A the Avogadro number and A and Z the mass and atomic number of the material (in this case air). The energy loss by bremsstrahlung is then described as [17]

$$E(X) = E_0 \exp\left(-\frac{X}{X_0}(1+b)\right) \tag{2.5}$$

with $X = \int \rho dz$ being the density-integrated thickness and $b = 1/\left(18 \ln\left(183/Z^{\frac{1}{3}}\right)\right) = 0.0122$ for air. So after a depth of $R = X_0 \ln 2$ an electron loses half of its energy.
For pair-production the integrated pair-creation probability is given by [17]

$$\mu(X) = 1 - \exp\left(-\frac{X}{X_0}\left(\frac{7}{9} - \frac{b}{3}\right)\right) \tag{2.6}$$

In Earth's atmosphere the radiation length is $X_0 = 36.7\,\mathrm{g\,cm^{-2}}$. Due to the varying density of the atmosphere one radiation length corresponds to different distances depending on the altitude. At sea level one radiation length corresponds to ≈ 300 m whereas at an altitude of 10 km, which is roughly the altitude of the maximum development of the shower, it corresponds to a distance of ≈ 1 km. This means that as an electromagnetic shower traverses deeper in the atmosphere its development accelerates. The altitude z_{max} where the shower reaches its maximum can be described as (assuming an isothermal atmosphere) [17]:

$$z_{max} = z_0 \log \frac{\rho_0 z_0}{X_0} - z_0 \log\left(\log\left(\frac{E_0}{E_c}\right)\right) \approx 9\,\mathrm{km} - 8.4\,\mathrm{km} \times \log\left(\log\left(\frac{E_0}{1\,\mathrm{TeV}}\right)\right) \tag{2.7}$$

Additional factors which play a part in the shower development are for example the multiple scattering of charged particles, which leads to a broadening of the shower, energy losses by ionization and atomic excitation or Earth's magnetic field, which broadens the shower in the east-west direction.

Hadronic Showers

Hadronic showers differ from electromagnetic showers in multiple ways. They are much more complex as several different processes can take place. Their development is dominated by strong interactions. Essentially, they can be splitted into two parts: a hadronic and an electromagnetic component (see Figure 2.8).

When a primary hadron scatters with atmospheric nuclei through strong interactions, it creates further particles such as pions and kaons (mesons) along with other nuclei. These secondary nuclei interact again with atmospheric molecules and create further hadrons. This interaction chain forms the hadronic part of the shower.

The decay of charged pions $\pi^{\pm}$ and kaons $K^{\pm}$, which have very short lifetimes so that no further interactions can take place, produces muons $\mu^{\pm}$ and neutrinos ν_{μ}. While the muons typically reach the surface of the Earth as they mostly interact through ionization, the neutrinos interact barley with matter and travel straight through Earth.

The electromagnetic sub-showers mainly originate from the decay of the neutral pion π^0 into two photons. From there they proceed through the mechanisms of pair-production and bremsstrahlung, as explained previously.

Due to the inelastic strong interactions the lateral spread of hadronic showers is larger than the spread of electromagnetic showers. The complex multiparticle processes involved in the development of hadronic showers also make them much harder to model in simulations.

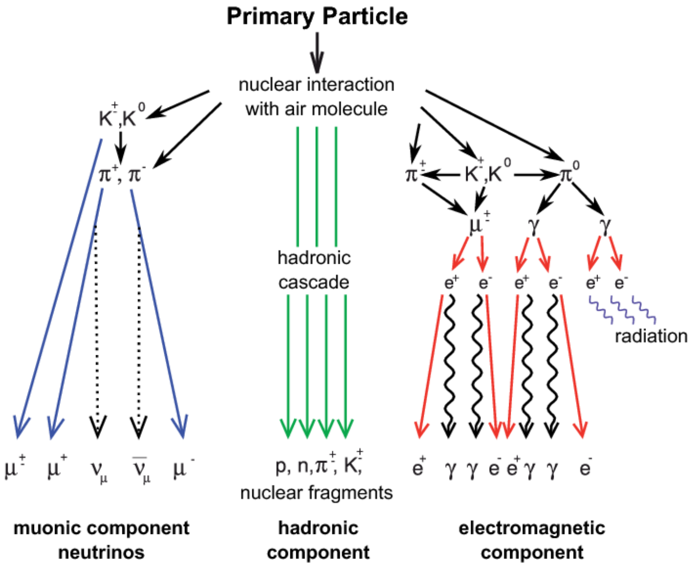

Figure 2.8.: Simplified model of the development of hadronic showers. [18]

2.2.2. Cherenkov Radiation

Charged relativistic particles traveling at a velocity v greater than the speed of light in the surrounding medium emit Cherenkov radiation. Although the speed of light in vacuum c forms an upper limit, its value can become smaller depending on the medium: $c_n = \frac{c}{n} < c$, with n being the refraction index of the medium. The refraction index of the atmosphere depends on the air pressure and therefore the altitude. At sea level c_n is about $0.997\,c$.
As a charged particle travels, it electrically polarizes the medium because of the particle's electric field. If the particle travels at a speed slower than the speed of light in the medium ($v < c_n$), the disturbance elastically relaxes as the particle moves on. However, if it travels fast enough ($v > c_n$), the particle moves forward faster than the response speed of the medium which means that a disturbance is left in the wake of the particle. The energy contained in this disturbance then radiates away as a coherent shock wave. This process are illustrated by Figure 2.9.
The Cherenkov light is emitted on a cone with a characteristic opening angle Θ between the light front and the particle's path

$$\cos\Theta = \frac{c_n \Delta t}{v \Delta t} = \frac{c_n}{v} = \frac{c}{nv} = \frac{1}{\beta n} \tag{2.8}$$

with $\beta = v/c$ [10]. This means that for an ultrarelativistic particle ($v \approx c \rightarrow \beta \approx 1$) the maximum opening angle Θ_{max} is

$$\Theta_{max} = \arccos\left(\frac{1}{n}\right) \tag{2.9}$$

Due to the variation of the refraction index of air with altitude, the opening angle increases from $\approx 0.2°$ at an altitude of 30 km to $\approx 1.5°$ at sea level. The diameter of the Cherenkov cone on the ground is given by

$$d = 2h \tan\Theta \approx 2h\Theta \tag{2.10}$$

where h is the altitude of the shower maximum. Typically diameters lie in the region of about 250 m.

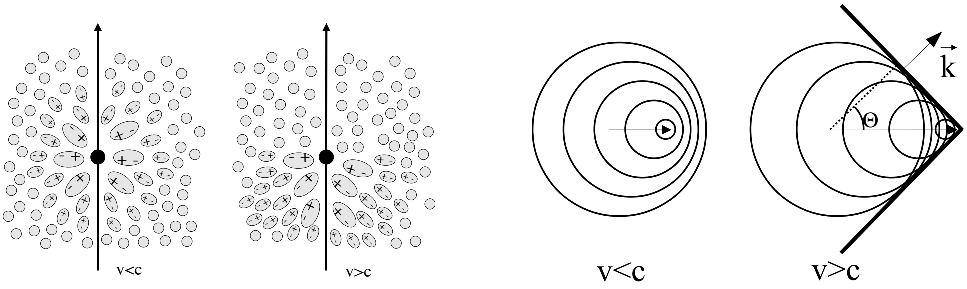

Figure 2.9.: Left: Illustration of the polarization of the medium by a relativistic particle. **Right:** Formation of a Cherenkov wave-front. [17]

The Cherenkov light cone of an electromagnetic shower has a homogeneous light distribution that slightly decreases towards the shower axis. Scattering processes of the secondary particles lead to a smearing of the light distribution.

For hadronic showers the Cherenkov cone looks different as the secondary particles in the shower are more widely spread. The electromagnetic subshowers lead to larger fluctuations in the Cherenkov light emission. Furthermore, the secondary $\mu^{\pm}$ often reach the ground emitting Cherenkov radiation on their path.

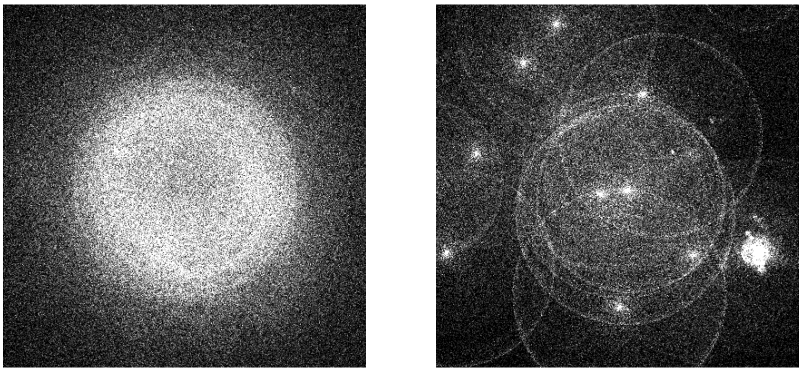
300 GeV γ-ray   1 TeV proton

Figure 2.10.: Lateral distribution of simulated Cherenkov light from air showers for different primary particles at 2200 m asl. The images correspond to a 400 m × 400 m area with the shower core at the center. [19]

2.2.3. Detection of Cherenkov Light with IACTs

The detection of high energy γ-rays with ground based telescopes is based on the imaging air Cherenkov technique. For a primary photon at 1 TeV energy, only about 100 photons per m^2 are seen on the ground, which all arrive in a time frame of a few nanoseconds. The photons are reflected by the mirrors of each telescope onto a camera consisting of multiple photomultiplier tubes (PMTs). The acquired images are used to deduce information about the primary γ-rays. In the following the main parts of an IACT shall be introduced and explained.

The optical system of an IACT has two main requirements to fulfill. The first is to make the mirror area as large as possible. This allows collecting more Cherenkov photons from each shower, which in turn lowers the energy threshold of the telescope. Typically the mirror form and surface quality has a much less important role than for optical telescopes, so that an optical point-spread function in the region of arcminutes is usually sufficient [20]. This is achieved by using tessellated reflectors, made up from hundreds of smaller mirror facets. The other requirement for the optical system is to make the field of view (FOV) as large as possible. The images produced from air showers are elliptical in shape (see Figure 2.11) and offset from the γ-ray source position in the field-of-view. The offset is proportional to the distance between the shower core projected onto the ground and the telescope (shower impact parameter). Therefore, even a point source on the sky requires a field of view of a few degrees and observations of extended sources even more.

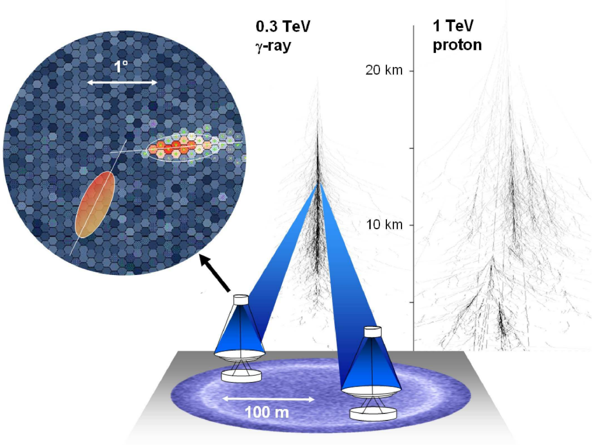

Figure 2.11.: Sketch of the imaging air Cherenkov technique showing the formation of an air shower from a 300 GeV γ-ray, production of Cherenkov light and the formation of an image in the telescope. [12]

Another integral part of an IACT is the camera. To cover a large enough FOV the camera itself has to be large (> 1 m). The photodetector pixels are made of PMTs as these have a good photon detection efficiency, a large detection area, nanosecond response time and a high signal amplification ($\sim 10^5$). All these factors are allowing them to resolve single photon signals. Figure 2.12 shows the PMT camera of the H.E.S.S. II telescope.

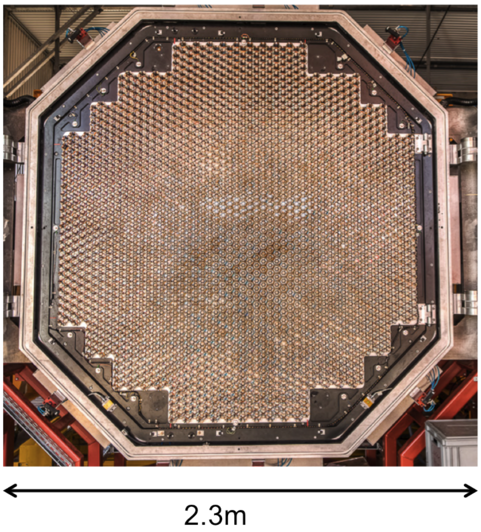

Figure 2.12.: PMT camera of the H.E.S.S. II telescope containing 2048 single PMTs with a pixel size of 42 mm (equivalent to 0.067°). [20]

The third important part is the trigger system. The arrival of Cherenkov flashes in the telescope is unpredictable and flashes, as already mentioned, last only a couple of nanoseconds. Additionally, as the flashes are in the optical range of the spectrum, they are overlaid by the night-sky background. Therefore it is highly impractical to monitor the sky continuously, which would mean sampling thousands of channels at high rates. Instead, the data acquisition system is only triggered during a small time period after the flash. Since the decision time is longer than the duration of the actual flash, the output signals must be delayed or continuously sampled and stored in memory buffers. There are several individual triggers. A typical requirement is that a minimum number of pixels exhibit a signal larger than a given threshold for a short period of time. In a system of telescopes it is also common to only trigger the readout if (at least) two telescope saw the same event. Once the signals are recorded and stored the system undergoes a short dead time of a few microseconds. The recorded data is usually splitted into runs with a duration between 20 min and 30 min.

When conducting an observation, different strategies are available. The simplest being so-called *on/off*-observations of a source. As the name already suggests, this means that alternating runs with the system pointing at the source (on-runs) and runs with the system pointing at an off-region (off-runs) are performed. The off-runs are then used to estimate the background in the on-runs. A more modern observation strategy is conducting observations in *wobble mode*. Instead of pointing directly at the source, several off-axis positions (typically at $\sim 0.5^\circ$ offset) around the source are observed in an alternating fashion. This allows to minimize differences in the detection sensitivity of the system. Additionally, it is possible to measure on and off data during the same run, therefore reducing the amount of observation time needed by half.

2.3. The H.E.S.S. Telescope System

Figure 2.13.: View of the full H.E.S.S. array with the four 12 m telescopes and the single 28 m H.E.S.S. II telescope [21]

The High Energy Stereoscopic System (H.E.S.S.) is a telescope array consisting of five Imaging Atmospheric Cherenkov Telescopes. It is situated in the Khomas Highlands in Namibia, about 100 km south-west of Windhoek, at 1800 m above sea level. The acronym is a tribute to honor Victor Hess who discovered cosmic rays in 1912. H.E.S.S. started operating in summer 2002 with one telescope (CT3) and was completed with the installation of the fourth telescope in December 2003. The array was upgraded with a fifth larger telescope (CT5), which started operating in July 2012. H.E.S.S. is designated to investigate VHE γ-rays in the energy range between 100 GeV and several tens of TeV.

The H.E.S.S. I telescopes

Phase I of H.E.S.S. consists of the four smaller 12 m sized telescopes. They are arranged in a square with a side length of 120 m, where one of the diagonals is orientated in the north-south direction. The spacing between the telescopes is a compromise between a large base length for good stereoscopic viewing and the condition that more than one telescope should observe an electromagnetic particle shower.

The mirror of each telescope consists of 382 round mirror facets of 60 cm diameter made of aluminized glass with a quartz coating. The total mirror area equals 108 m^2 per telescope, while the focal length is 15 m. Each mirror is focused for an object distance of about 10 km, which is approximately the altitude of the maximum of an air shower. The cameras of the four telescope consists of 960 PMTs with a pixel size of 42 mm (equivalent to 0.16°). The total field of view of the camera is 5°. The total weight of each telescope is about 60 t.

The H.E.S.S. II telescope

Phase II of H.E.S.S. describes the commission of single large 28 m sized telescope (CT5). It was added at the center of the array and increased the energy coverage, sensitivity and angular resolution of the array. The mirror uses a parabolic shape and is made out of 875 hexagonal facets each 90 cm (flat-to-flat) in size. Like the H.E.S.S. I mirror facets, they are made of quartz-coated aluminized glass. The mirror has a total area of 614 m^2 and a focal length of 36 m. The camera follows the H.E.S.S. I design, only being much larger. It has 2048 PMTs each grouped in 16-PMT drawers, which contain the signal storage, digitization, triggering and readout. The pixel size is 42 mm (equivalent to 0.067°) while the field of view is 3.2° on the sky. CT5 weighs about 580 t.

3. Sensitivity Tool

Now that the basic principles of γ-astronomy have been presented, this chapter focuses on the sensitivity software tool which was developed over the course of this thesis. The tool's intention is to quickly, without the need of a full analysis, determine the sensitivity of H.E.S.S. when observing a certain source under given conditions. Aside from the functionality of the tool, other necessary topics like the applied background model, the verification of the results or the limitations of the tool will also be discussed here.

3.1. Sensitivity

Before presenting the sensitivity tool in detail, first the term "sensitivity" in the context of IACTs shall be explained.

Sensitivity refers to the minimal flux from a source required in order to make a detection in a given amount of time. The flux of a source is defined as

$$F = \frac{dN}{dA dt} \tag{3.1}$$

where N is the number of detected events, A the effective area and t the observation time. The significance S of a signal can be described by

$$S = \frac{N_\gamma}{\sqrt{N_{bkg}}} \tag{3.2}$$

with N_γ and N_{bkg} being the number of detected γ- and background-events. This is a simplified and practical approach. It provides good enough results and is often used for sensitivity calculations. However, a more accurate calculation can be achieved with the adaptation of Equation 17 from Li & Ma [22] which is usually used to claim discoveries.

Combining and rearranging equations 3.1 and 3.2 results in the γ-ray sensitivity

$$F_\gamma = \frac{S\sqrt{\dot{N}_{bkg}}}{A_\gamma \sqrt{t_{obs}}} \tag{3.3}$$

In astroparticle physics the statistical significance of an event is expressed in multiples of the standard deviation or sigma (σ) of a normal distribution. Typically an event is called a

detection when a significance threshold of $S \geq 5\sigma$ is reached. This means that the probability of a “false alarm” is less than 3×10^{-7}.
When referring to the sensitivity of an instrument, one distinguishes between differential and integral sensitivity. The differential sensitivity is an important quantity when investigating spectral features such as cutoffs or breaks. It describes the sensitivity at a certain energy. The integral sensitivity over a relevant energy range, however, is related to the potential of an instrument to discover new sources.
Figure 3.1 shows the differential sensitivity of H.E.S.S (among others) for a 100 h observation. The parabola-like shape of the sensitivity curves is a result of two different factors at different energies. At lower energies the sensitivity is limited by the ability to trigger the detector. The γ-rays might not be energetic enough to produce enough Cherenkov light in the atmosphere. Another important factor is the worse gamma/hadron separation of the system at lower energies. In the higher energy regime the sensitivity drops, because of the limited effective area of the detector. As the γ-ray flux becomes smaller at higher energies, the detection probability is strongly dependent on the size of the detector.

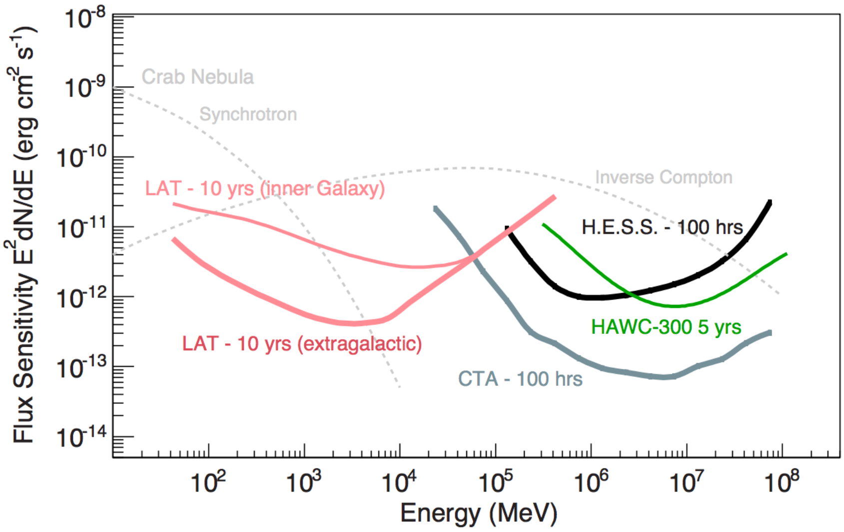

Figure 3.1.: Differential sensitivity (technically the integral sensitivity per energy bin) of different instruments (H.E.S.S., Fermi-LAT, HAWC, CTA). A minimum significance of 5σ in each bin and at least 10 events per bin where required. [11]

3.2. Sensitivity Tool

The purpose of the tool, as previously mentioned, is to provide a quick way of calculating the sensitivity for any sky position without the need of running the full H.E.S.S. Analysis Program (HAP). If H.E.S.S. runs are already available for the position, the tool should calculate the already observed sensitivities. This provides information to whether the new source should or could have already be seen with H.E.S.S. If no runs are available though,

a set of parameters could be specified within the tool that define the planned observation characteristics. This way an estimation of the sensitivity can also be calculated.
The tool is based on *ROOT*[2] which is a data analysis framework for particle physics developed by CERN and written in C++. The tool also uses methods from the HAP framework[3].

3.2.1. General Structure

In the following, the general structure of the tool shall be explained and is displayed in Figure 3.2.

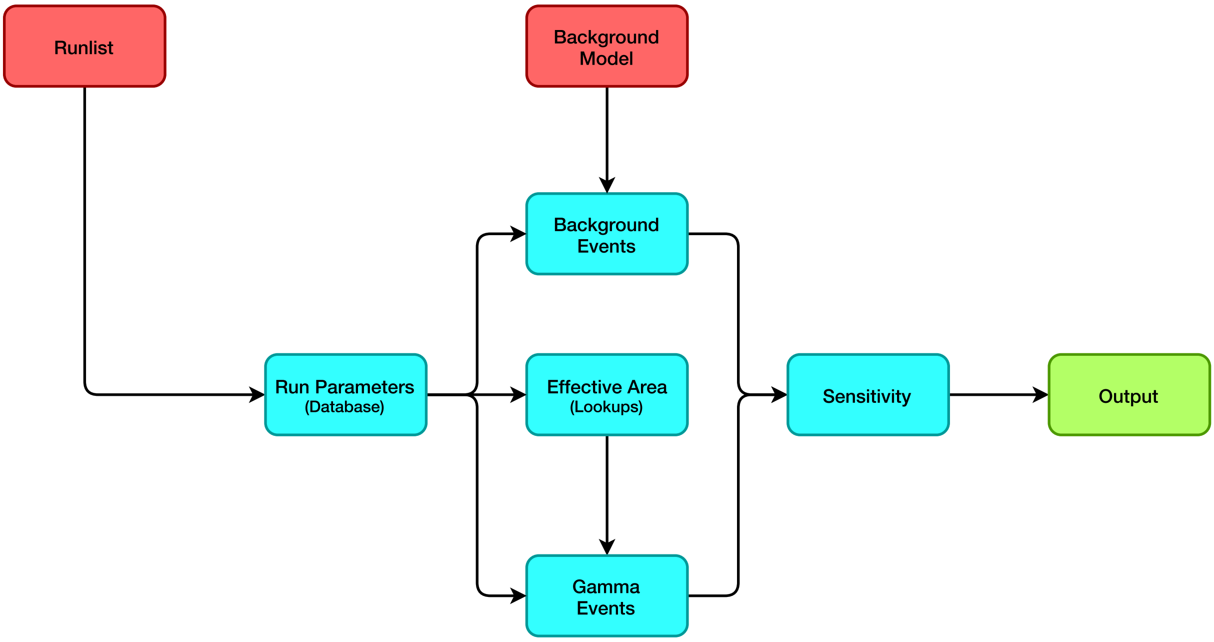

Figure 3.2.: Flowchart representing the procedure for calculating sensitivities of the developed tool. Input is represented in red, internal operations in blue and output in green.

The tool requires two different types of input: a list of H.E.S.S. observation runs and a ROOT file containing background data stored in 3-dimensional histograms. Also, some additional parameters, which can be found in Table 3.1, need to be set.
The first step is to extract several run related parameters from the H.E.S.S. database. These are the date of the run, the muon phase[4], the live time, the zenith angle and the target- and pointing position. As these parameters are essential for the calculations in the script, they can also be set manually in case no runlist can be provided. The next step is to compile all necessary data needed for the sensitivity calculation. This includes the calculation of

---

[2] Software version 5.28

[3] Software version ICRC-2015

[4] The muon phase defines the optical efficiency of each H.E.S.S. telescope.

background events based on the provided background model, as well as the creation of a lookup histogram of the effective area, which is needed for the calculation of the γ-events. These steps are done for each run individually before their results are then combined. The final step is the calculation of differential (technically integral sensitivity per energy bin) and integral sensitivities. The output of the tool is again a ROOT file with several histograms containing the results of intermediate calculations and the sensitivities.

The output histograms, as well as the histograms the tool handles internally, all exhibit the same structure. A binning of five bins of energy per decade is used with a range of $-2.0 < \log(E\,[\mathrm{TeV}]) < 2.2$. This results in a total of 21 bins. It is, however, possible to change the binning the tool uses to ones liking.

Parameter Name	Explanation	Standard Value
thetaSqr	θ^2-cut value	0.0125
count_thres	Minimum number of signal counts per bin	10
ratio_thres	Minimum signal/noise ratio per bin	0.05

Table 3.1.: Parameters needed to be specified in the script.

3.2.2. Calculating γ-Events

For the sensitivity calculation an estimation of the total number of photons or γ-events N_γ is necessary. The Crab nebula is the strongest γ-ray source in the sky and therefore often used as a standard candle in γ-astronomy. For this reason the estimation of N_γ is based on its spectrum as published in Aharonian et al. (2006)[23]

$$\frac{dN_\gamma}{dAdEdt} = 3.76 \times 10^{-7} \times E^{-2.39} \times \exp\left(\frac{E}{14.3\,\mathrm{TeV}}\right) \frac{1}{\mathrm{s\,m^2\,TeV}} \tag{3.4}$$

The spectrum describes the flux of photons per area per time and per energy. In order to receive the correct total number of photons N_γ corresponding to the individual observation run, the flux has to be multiplied by the live time and the effective area of the run. The latter is calculated by methods from the HAP framework which, depending on the run parameters, returns a histogram of the effective area for each run. Lastly, the flux needs to be integrated over the width of each energy bin.

For each energy bin i, the script ultimately calculates the number of γ-events $N_{\gamma,i}$ in the following way

$$N_{\gamma,i} = t_{live} \times A_{eff,i} \int_{E_{i,low}}^{E_{i,up}} \frac{dN_\gamma}{dAdEdt} dE \tag{3.5}$$

whereas $E_{i,low}$ and $E_{i,up}$ are the lower respectively the upper edge of each energy bin. t_{live} corresponds to the live time of each run. The result is a histogram that contains the number of γ-events per energy bin for each observation run. Ultimately, these histograms are summed up to receive the number of gammas per bin for the whole runlist.

This approach should yield a reasonably well estimated number of photons. Though, it also comes with a few possible error sources. Firstly, the estimation of gammas is based on the above Crab nebula spectrum. It has a spectral index of $\Gamma = 2.39$ and an exponential cutoff at 14.3 TeV. Analyzing a source that differs vastly from this spectral shape will consequently yield inaccurate results. Secondly, the effective area term $A_{eff,i}$ would correctly be required to be included within the integral. However, the effective areas exist in a binned form meaning one assumes a constant value within each bin. This means that with increasing bin sizes the stored value in the respective bin becomes less and less representative for the corresponding energy. It is not expected that the binning used in this thesis yields any major issues on this matter.

3.2.3. Calculating Background Events

The number of background events required for the sensitivity calculation is extracted from a background model developed by M. Mayer and published on the H.E.S.S. confluence pages [24]. In this section first the general approach that is used to model the γ-like background shall be explained. Afterwards the method used to extract the correct background information from the model is presented. In the end, some verification of the used methods and the extracted background will be shown.

General Approach

The background model uses galactic and extragalactic H.E.S.S. I off-runs with at least three participating telescopes. If necessary, appropriate exclusion regions are applied, so that there are no known sources in the field of view. These runs are divided into groups of altitude and azimuth (see Table 3.2) based on their pointing. The underlying assumption of the model is that runs within the same altitude-azimuth group exhibit similar background shapes and spectra. While in reality the background of each run is also dependent on the individual observation conditions, these factors should average out when combining enough off-runs. In the next step all runs within a group are stacked together in a three-dimensional cube of detector coordinates (DetX, DetY) and energy ($\log E$). Depending on the available statistics the spatial binning and energy binning changes. For the groups with the most statistics a $60 \times 60 \times 20$ binning is used, while it can decrease to $15 \times 15 \times 5$ for groups with the lowest statistics (when there is less than 5 h of off data). Since the least statistic is available for runs with low altitude angles, where the energy threshold is high, the decrease in energy binning should not be a problem. In order to reduce statistical noise and bin-by-bin fluctuations, the model is then spatially smoothed for each energy bin. The final result of these steps is a background template for each altitude-azimuth group which contains the specific background rate (in $\mathrm{MeV^{-1} sr^{-1} s^{-1}}$) for each detector position and energy. The template is saved in a *FITS*-file.

Altitude bins (bin edges)	$[0, 20.5, 22.0, 24.0, 26.0, 28.5, 32.5, 37.5, 42.5, 47.5, 55.0, 65.0, 80.0, 90.0]^\circ$
Azimuth bins	0°, 180°

Table 3.2.: Altitude and azimuth binning used in the model for H.E.S.S. *std*-cuts.

Figure 3.3 shows the energy distribution of background rates within an altitude range of $[37.5, 42.5]^\circ$ and azimuth of 180° for different positions in the camera (offsets) as an example. While in the lower energy regime higher offsets lead to lower background rates, this behavior is reversed for higher energies $\gtrsim 10\,\mathrm{TeV}$. The reason can be seen in Figure 3.4, which shows the distribution of background rates in the camera as a map. At lower energies the point of maximum background rates lies in the center of the camera. For higher energies this point shifts towards the edge of the camera and leaves a "hole" of lower rates in the center. This effect might be caused by the shower geometry and the size of the camera, though it was not examined in detail in this thesis. At higher energies showers become bigger in size. If such a shower hits the center of the camera, it will not fit fully inside the camera and therefore will be cut off at the edge. The shower then cannot be reconstructed correctly and will be discarded by the analysis.

At lower energies, showers can only be detected up to a maximum impact parameter. As they contain much less photons than showers at higher energies, a larger impact parameter causes a decrease in photon density which at some point becomes too small to trigger upon.

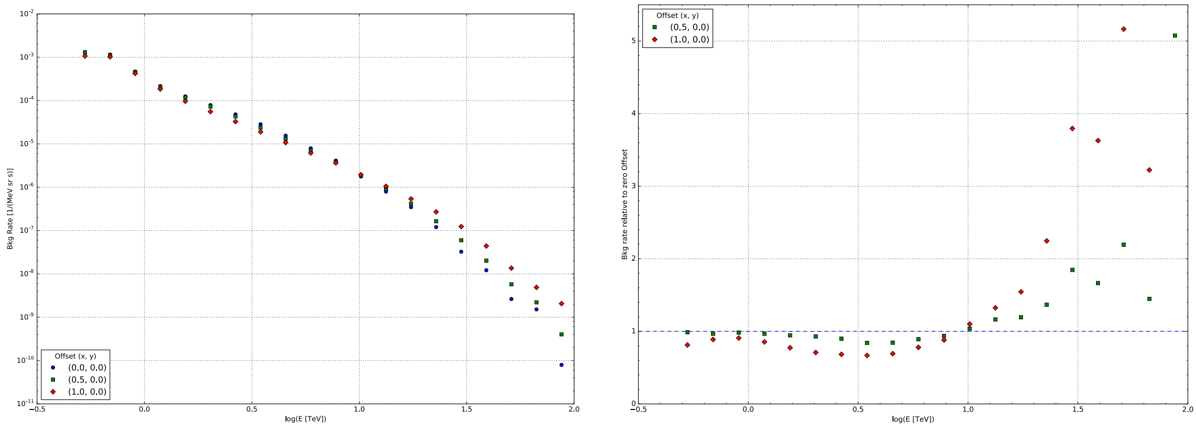

Figure 3.3.: Energy distribution of the background rates from the model ($[37.5, 42.5]^\circ$ altitude, 0° azimuth) for different positions in the camera (**left**) and differences in rates relative to zero offset (**right**). The highest energy point for 1.0° offset has been excluded from the right plot to allow a sensible scaling.

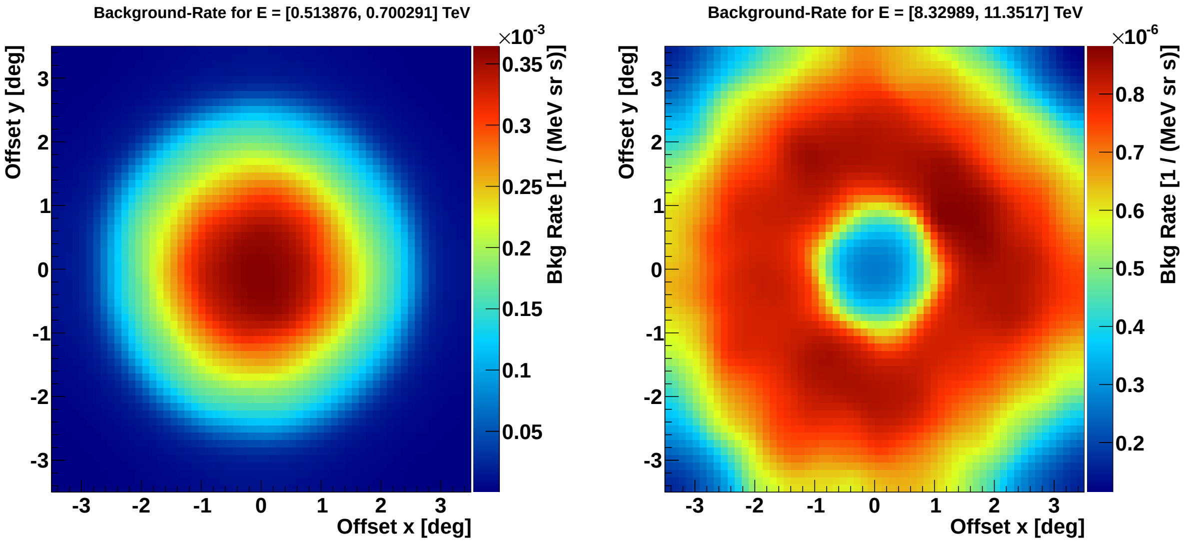

Figure 3.4.: Distribution of background rates in the camera for an energy range of roughly $[1.0, 1.34]$ TeV (**left**) and $[11.5, 15.0]$ TeV (**right**). The data corresponds to $[80.0, 90.0]^\circ$ of altitude and 180° of azimuth.

Extracting the Background from the Model

One essential part of the sensitivity tool is to extract the background information from the model and calculate the correct amount of background events for each observation run.

Following the extraction of all relevant run parameters from the H.E.S.S. database, the first step of the background calculation is to determine in which altitude and azimuth bin of the background model the run falls and what offset position the source has in the detector. The altitude and azimuth bin is obtained by transforming the pointing position of the run from the equatorial coordinate system (RADecJ2000) to the horizontal system (AltAz) based on the date of the run and the coordinates of the H.E.S.S. site, which are stored in the HAP software. The offset is defined as the difference between the pointing position of the run and the target (i.e. source) position. However, as the offset is needed in detector coordinates another coordinate transformation into a two dimensional system is needed. The background model uses the so called nominal system. The x and y component of the vector between pointing and target position in the nominal system correspond to the x and y position in the camera.

Once it is clear at what altitude and azimuth the source lies and where it is located in the camera, the background for the source is calculated. The method used here is inspired by the ring-background model [25] which uses a ring around the source position in celestial coordinates as *OFF*-region to estimate the background (see Figure 3.5). One problem with this approach is that it requires an acceptance correction. The system acceptance is defined as the probability of accepting a background event (after triggering, analysis cuts and γ-ray selection) reconstructed at a certain position in the FoV with a certain energy. It is a reasonable assumption that the acceptance is radially symmetric [25]. The left background map in

Figure 3.4 shows the resemblance to a radial symmetric distribution. Since the the ring of the ring-background model covers different offset positions in the camera, the acceptance can not be assumed to be constant so that a correction is required.

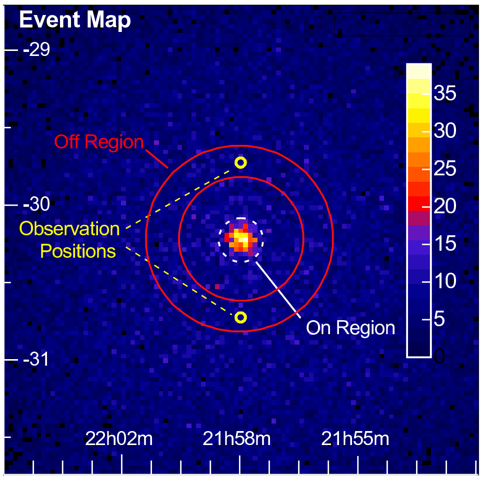

Figure 3.5.: Schematic illustration of the ring-background model for a count map (in celestial coordinates) of γ-ray-like events from 5 h of H.E.S.S. data of PKS 2155-304. The observations were done in wobble mode with offsets of ±0.5° in declination. [25]

In order to circumvent this problem the background in the sensitivity tool is extracted in the following way: First, the background rates stored in the bin at the position of the source in the camera and its eight neighboring bins are examined. From this 3×3 grid of bins the minimum and maximum background rates are used to define a selection range. During the next step, the tool loops over the whole FoV in the camera and selects every bin whose background rate is within the specified range. As the distribution of background rates resembles a radial symmetric distribution about the camera center, a ring-like structure of bins emerges (see Figure 3.6, right) as *OFF*-region. These bins are also all located at roughly the same offset from the camera center, so that a constant acceptance can be assumed and no further correction needs to be applied. However, the overall method should in principle also work for a non symmetrical distribution of background rates. The criteria for choosing the bins already implies similar acceptance levels.

To ensure that the background rates from the bins in the 3×3 grid are representative for all selected bins, meaning their distribution is not skewed in any way, the mean background rates from both have been compared. An example is presented in Figure 3.6 (left). The mean background rate of the selected bins is shown by the black line with the shaded black area representing its error range. Likewise, the red line and area displays the mean rate and its error from the bins in the 3×3 grid. Both values are nearly identical making them hard to distinguish in the plot. The mean rate from all selected bins is $2.1133(29) \times 10^{-4}\,\mathrm{MeV^{-1}sr^{-1}s^{-1}}$ while the mean rate from the bins in the grid is $2.113(25) \times 10^{-4}\,\mathrm{MeV^{-1}sr^{-1}s^{-1}}$. It is no surprise that the error on the latter is significantly larger as the sample size is much smaller (9 vs. 65 bins). This test has also been performed for different altitude and azimuth ranges and at different energies with similar outcomes. Overall this means that the bins in the grid represent the whole selection of bins reasonably well and consequently that the selection method is an adequate approach of extracting the background data from the model.

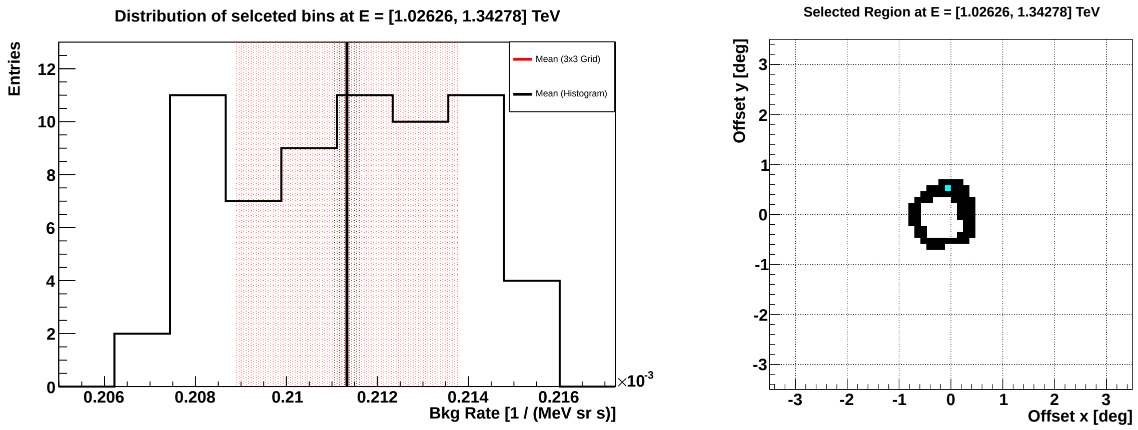

Figure 3.6.: Plots addressing the selection of bins for the background estimation for an altitude range of $[42.5, 47.5]^\circ$, azimuth of 0° and energy range of $[1.0, 1.34]$ TeV. **Left:** Distribution of the background rates for 65 selected bins. The black line represents the mean value of the histogram with respective error range while the red line (overlaid by the black one) and area shows the mean of the bins in the 3×3 grid. The mean values are nearly identical showing that the bins in the are an accurate representation of the selected bins. **Right:** Map of the selected bins' location in the camera. The blue bin represents the source position at 0.5° offset. The selected bins have roughly the same offset from the camera center and form a ring-like structure.

The last step of the background calculation is to convert the rates (in $\mathrm{MeV}^{-1}\mathrm{sr}^{-1}\mathrm{s}^{-1}$) from the selected bins to actual background events corresponding to the individual H.E.S.S. run. Therefore the average background rate per bin is calculated by dividing through the number of selected bins n. This average rate is then integrated over the width of the respective energy bin and multiplied by the live time of the run t_{live}. In order to receive the correct amount of background events the rate also needs to be normalized to the area of the *ON*-region of the source. This area is essentially defined by the chosen Θ^2-cut. In mathematical terms, the calculations can be expressed through

$$N_{bkg} = t_{live} \cdot \left(\pi \Theta^2\right) \cdot \frac{1}{n} \int\limits_{E_{i,low}}^{E_{i,up}} \left(\sum_{j=1}^{n} \frac{dN_{bkg,j}}{dA_{on}\,dt\,dE} \right) dE \tag{3.6}$$

where $E_{i,low}$ and $E_{i,up}$ are the lower respectively the upper edge of each energy bin. A_{on} in this context refers to the size of the ON-region in the sky.

The background is determined for every energy bin for every provided run individually. Once all runs from the runlist have been processed their background estimates are combined to obtain a background estimate representing the whole runlist.

Verification and Energy Thresholds of the Background

Now that a method has been established to extract the background from the model the next necessary step is to verify the results of this method. To this purpose the background counts calculated by the sensitivity tool are compared to those coming from the HAP analysis (*std*-cuts). For each combination of altitude and azimuth ranges runlists comprising 20 runs ($\approx 8-10$ h of data), preferably of well known sources like PKS 2155-304 or the Crab nebula, have been created. Only for low altitudes, where statistics are low, shorter runlists have been used.

Some results of this verification are shown in Figure 3.7, but the following observations are relevant for all conducted comparisons. The plots in the figure show the energy distribution of background events. The top row shows the initial output of the model in comparison with HAP. In the mid energy range (roughly between 1 TeV and 10 TeV) both histograms are in good agreement, apart from some individual deviations, which are most certainly a result of statistical fluctuations as the runlists' live times are still relatively low. Above $\approx$ 10 TeV, where the number of background events is smaller than one event per bin, the deviations get bigger with single bins experiencing up to three times less events than HAP. While these differences are probably still the consequence of low statistics, because one expects generally fewer background events at higher energies and again because of the limited live times of the runlists, it is also noteworthy that the results from the model extend up to higher energies than HAP.

From the plot it is also immediately apparent that at lower energies the model and HAP produce vastly different amounts of background events with differences of 40 % and higher. A possible reason for this behavior are different cut configurations between HAP and the model. These lead to different lower energy thresholds. Because the results from the model are therefore not reliable in this energy region, lower energy cuts are additionally implemented in the model. To determine the energy (or energy bin) at which the threshold should be set, the allowed tolerance between the background events from HAP and the model is set to ±20 %. Energy bins which exhibit a greater difference will simply be cut off. These thresholds are defined for each combination of altitude and azimuth ranges. The bottom row of histograms in Figure 3.7 shows the background events from the model after the applied cuts in comparison to HAP.

After the initial energy thresholds have been defined, a second stage of verification is performed. Now the runlists are "mixed", which means their runs do not exclusively lie in a single altitude bin, but span over a wider altitude range. The runlist are also larger with total live times up to 23 h. The results for two runlists are displayed in Figure 3.8. These underline the previously made observations: The number of background events extracted from the model is in very good agreement with the HAP numbers up to energies of about 15 TeV while the applied energy threshold cuts make sure that discrepancies at the lowest energies are eliminated.

On the basis of the “mixed” runlists the initially set lower energy thresholds were further refined which resulted in higher thresholds for some altitude-azimuth bin combinations. Generally the thresholds are on the conservative side. The final set of thresholds is displayed in Table 3.3.
The observations taken from the verification steps of the calculated background are already a good indication of the energy range in which the sensitivity tool produced valid results. Further elaborations concerning this subject will be done in the following section.

Altitude	0° Azimuth		180° Azimuth	
	Bin	Energy [TeV]	Bin	Energy [TeV]
26.0 - 28.5°	12	1.58	-	-
28.5 - 32.5°	13	2.50	13	2.50
32.5 - 37.5°	12	1.58	12	1.58
37.5 - 42.5°	11	1.00	12	1.58
42.5 - 47.5°	11	1.00	11	1.00
47.5 - 55.0°	10	0.63	10	0.63
55.0 - 65.0°	10	0.63	10	0.63
65.0 - 80.0°	10	0.63	10	0.63
80.0 - 90.0°	10	0.63	10	0.63

Table 3.3.: Lower energy thresholds applied during the background calculation for each altitude-azimuth combination. For altitudes $< 26.0°$ and the combination of 26.0-28.5° altitude at 180° azimuth no data from the background model is available.

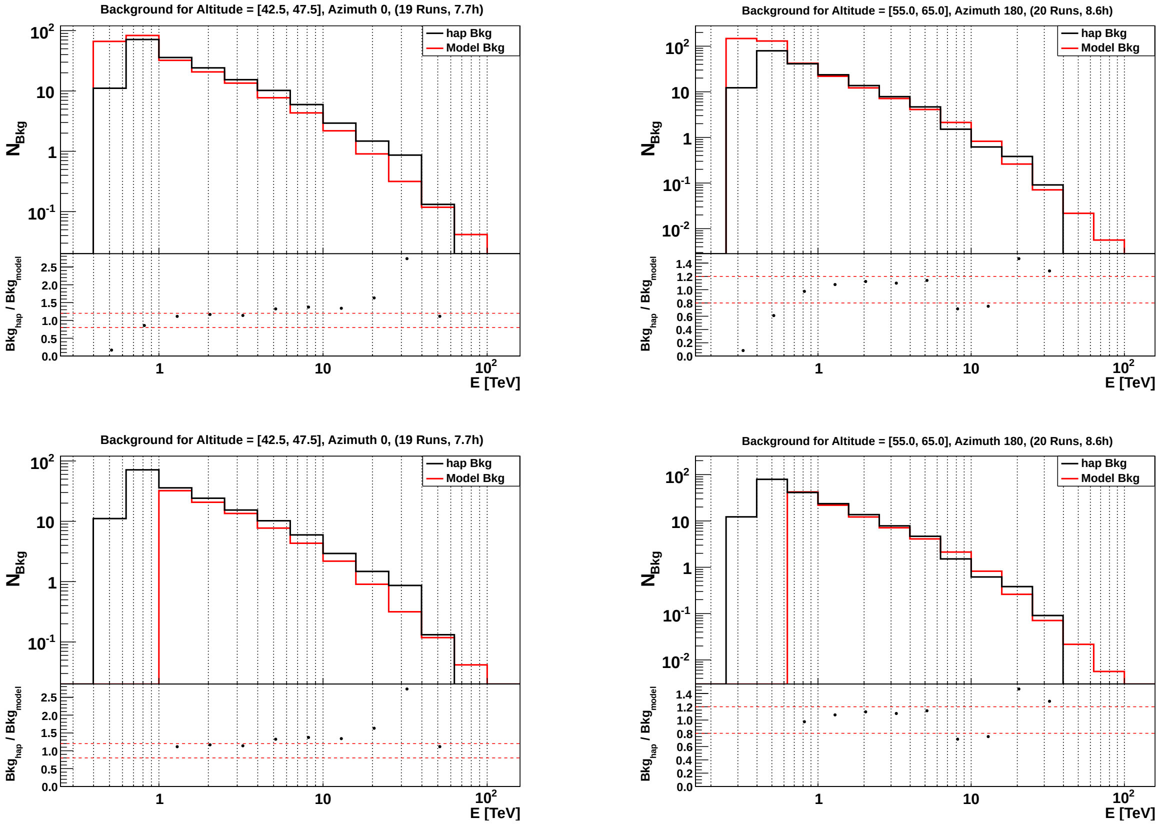

Figure 3.7.: Comparison between the calculated background events from the model and HAP-analysis (*std*-cuts). The histograms on the **left** show the background for an altitude range of $[42.5, 47.5]^\circ$ and azimuth of 0°. The background was calculated based 19 runs of the Crab nebula (7.7 h). The **right** histograms represent an altitude range of $[55, 65]^\circ$ and azimuth of 180° and are based on 20 PKS 2155-304 runs (8.6 h). The **top row** of histograms are prior to the application of lower threshold cuts for the model while the **bottom row** have the cuts already applied.

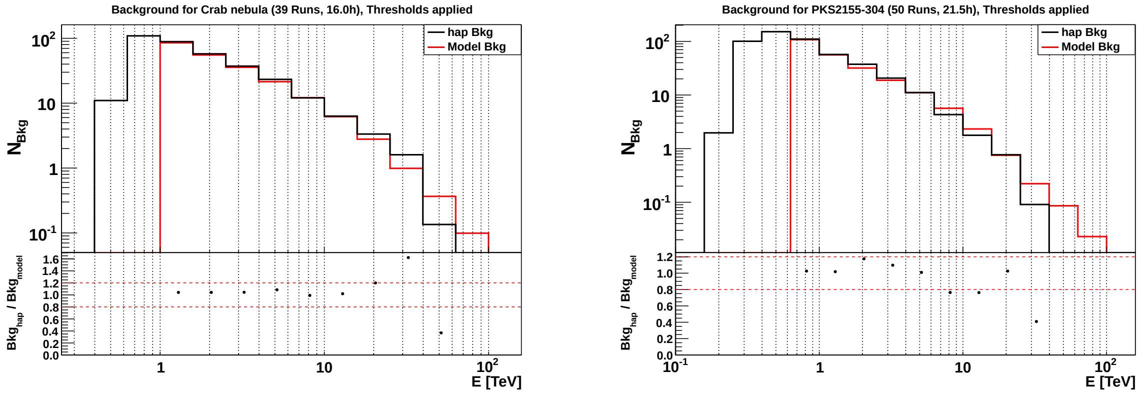

Figure 3.8.: Comparison between the calculated background events from the model and HAP-analysis (*std*-cuts) for runlists covering wider altitudes ranges and higher live times. The background events in the **left** histograms are calculated for 16.0 h of data on the Crab nebula with an altitude range of $[37.5, 47.5]°$, while the **right** histograms are made for 21.5 h of data on PKS 2155-304 with an altitude range of $[47.5, 80.0]°$.

3.3. Verification of the Sensitivities

During the previous chapters the functionality of the sensitivity tool has been explained as well as that of the applied background model. Additionally the interim results of the background calculation have been checked. The final step missing to demonstrate the functioning of the sensitivity tool is the verification of the sensitivities itself. This shall be presented here. For the sensitivity verification the same “mixed” runlists as for the background checks were used as these provide a relatively good sample of runlists used in publications with large enough live times and a wider distribution of altitude coordinates. Figure 3.9 displays the differential sensitivities from the tool in comparison to the ones derived from HAP. In fact, the presented sensitivities are not differential but so called “pseudo-differential” sensitivities meaning they are actually integral sensitivities calculated for each energy bin (for five bins per decade). Similarly as for the background events, the sensitivities are in very good agreement to the results from HAP with deviations in the region of ±15 % for energies up to about 15-20 TeV. At energies above 20 TeV the calculated sensitivities become more inaccurate as either the differences to HAP get bigger, or there is no HAP data available for a comparison.

The sensitivity curves exhibit the same behavior as the histograms of the number of background events when compared to HAP which suggest that the accuracy of the background model and the extraction method are the limiting factors for the sensitivity estimation.

A common value for the nominal sensitivity of the H.E.S.S. I array cited in publications is $2.0 \times 10^{-13}\,\mathrm{ph\,cm^{-1}s^{-1}}$ for a 25 h observation at zenith (0° zenith angle) of a point-like source detected at a significance of 5σ [26]. This is equivalent to 1 % of the Crab nebula flux above 1 TeV [23]. Besides the “pseudo-differential” sensitivities the tool is also capable to produce integral ones. This has been utilized to compute a comparing value for similar observation conditions. According to the tool the integral sensitivity above 1.25 TeV reached in the same amount of time is $2.22 \times 10^{-13}\,\mathrm{ph\,cm^{-1}s^{-1}}$ for a point-like source at a zenith angle between 0 - 10° at an offset of 0.5° in the camera (typical wobble offset). Thus, the two sensitivity values are in good agreement and only off by about 11 % for slightly different conditions. The exact parameters used to calculate the nominal sensitivity value can be found in Appendix A.1.

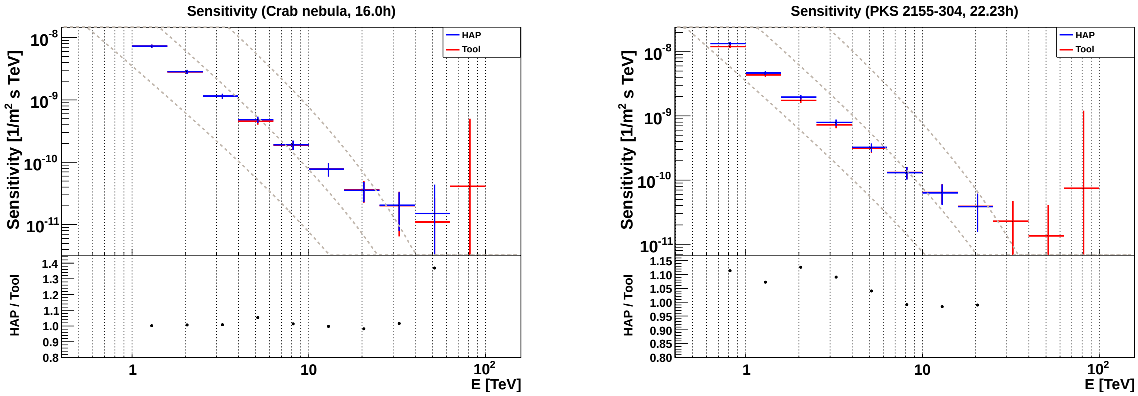

Figure 3.9.: Pseudo-differential sensitivities (integral sensitivities for five bins of energy per decade) for 16 h of data on the Crab nebula (**left**) and 22.2 h of data on PKS 2155-304 (**right**). The sensitivities calculated from the tool are compared to the ones derived from the HAP analysis. The dotted grey lines represent 1 %, 10 % and 100 % of the Crab nebula flux.

4. Analyzing 3FHL Data

After establishing that the sensitivity tool works as intended, in this chapter it is brought into use. The intention is to find hard γ-sources observed by the Fermi-LAT and investigate whether these sources have already been seen with H.E.S.S. or could be potential new targets for follow-up observations.

The Fermi-LAT (Large Area Telescope) is the main instrument of the Fermi Gamma-ray Space Telescope (FGST) which was launched into low Earth orbit on 11 June 2008. The LAT is an imaging high-energy γ-ray telescope covering an energy range from about 20 MeV to more than 300 GeV, therefore making it an ideal low-energy counterpart for H.E.S.S. (100 GeV to several TeV). With its large field of view, it is able to see 20 % of the sky at any given time and observe the entire sky every three hours. In order to detect cosmic γ-rays, the incoming photon is converted into a electron-positron pair. By tracking the path of the electron and positron inside the detector and measuring their energy with a calorimeter, the LAT is able to reconstruct the arrival direction and energy of the primary photon.

The data taken by the Fermi-LAT is grouped together and released in source catalogs. The study presented in this thesis is done with an internal and preliminary version of the *3FHL* catalog. It is a summary of 7 years of Pass 8 data in the energy range of 10 GeV to 2 TeV. Pass 8 corresponds to the version of the data implying things like instrument simulations, event selection and reconstruction, instrument response functions, systematic uncertainties and more. The 3FHL catalog contains a total of 1720 sources with 145 of them being already detected by IACTs (association in TeVCat [27]). 358 sources are new, meaning they have now association in 1FHL, 2FHL, 3FGL or TeVCat. Therefore there are plenty of potential targets for H.E.S.S. follow-up observations.

In this chapter the analysis of the 3FHL data is presented which includes the categorization and selection of sources, the calculation of sensitivities with the sensitivity tool for these sources, as well as a discussion of the final results.

All following sensitives are calculated with an ON-region size of $\Theta^2 = 0.0125\,\mathrm{deg}^2$ corresponding to HAP *std*-cuts.

4.1. Source Categorization

As already stated, the 3FHL catalog contains a total of 1720 sources. Not all of these sources are observable with H.E.S.S. or may have already been observed. The first task therefore is to reduce the data set in a sensible way. At first all sources whose declination angle was outside the range of $-73° < \mathrm{Dec} < 27°$ were discarded. As H.E.S.S. is located at roughly

23°S latitude, this means all sources with a zenith angle greater than 50° and therefore not observable with H.E.S.S under reasonable conditions are discarded. A second criteria used to classify the sources is the ideal integral sensitivity of H.E.S.S. above 1 TeV for a 30 h observation. The sensitivity tool was used to calculate a value of $2.119\,52 \times 10^{-13}$ ph cm^{-1}s^{-1} for these conditions. The exact parameters used to derive this value can be found in the Appendix A.1.

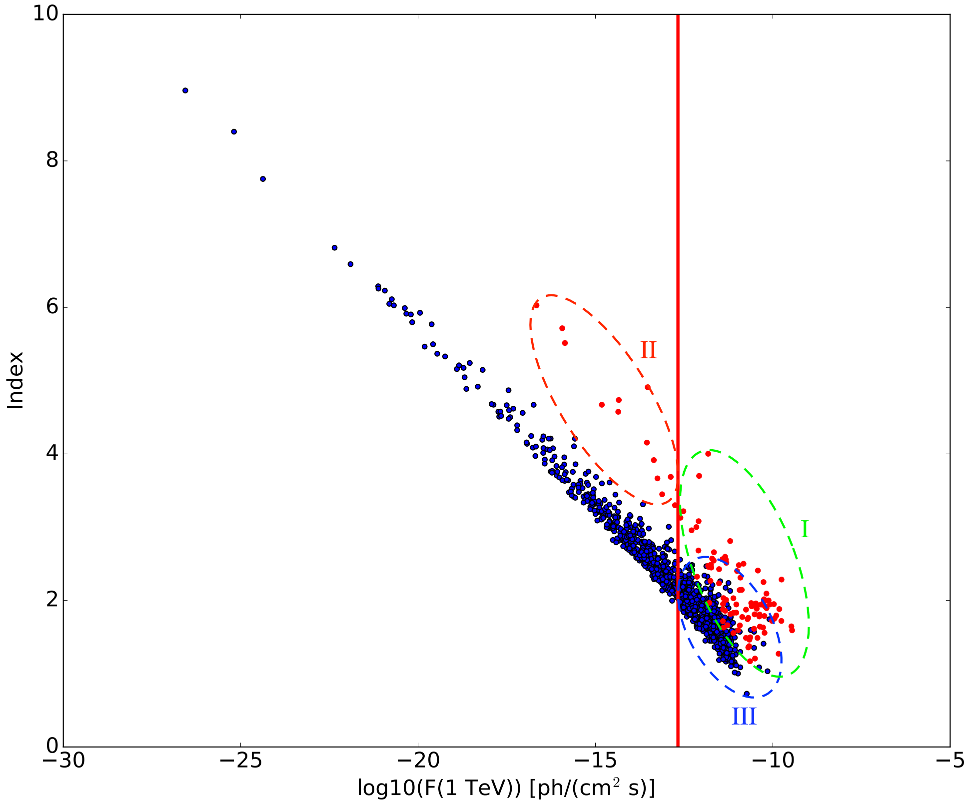

Figure 4.1.: Extrapolated flux above 1 TeV for all 3FHL sources observable with H.E.S.S. under a zenith angle of < 50° with respect to their spectral index. Blue dots represent sources without any association in TeVCat or the H.E.S.S. Galactic Plane Survey (HGPS), while red marked sources are found in TeVCat. The vertical red line marks the calculated value for the integral sensitivity of H.E.S.S. above 1 TeV for a 30 h observation. The sources are divided into three groups: already seen and understood sources (I), sources that despite being deemed as "not observable" have still been seen (II) and potential candidates for follow-up studies. (III).

The results of this first categorization are displayed in Figure 4.1 which contains all 3FHL sources observable with H.E.S.S. under zenith angles of < 50°. In it the extrapolated flux above 1 TeV of each source is plotted against its spectral index. The extrapolation was done using a simple power law $dN/dE \sim E^{-\Gamma}$. At his point it is noteworthy that, because the further analysis of this thesis depends on the quality of this extrapolation, a limiting factor is the accuracy with which Fermi has measured the spectral index of each source. Blue marked sources in the plot have no association in TeVCat or the H.E.S.S. Galactic Plane Survey (HGPS), while the red ones are found in TeVCat. The vertical red line represents the integral sensitivity from above and acts as a divider. This plot forms the baseline for any further analysis in this thesis. Accordingly, the 3FHL sources are split into three different classes:

I. Sources in this class have already been seen with H.E.S.S, which they are also expected to be (red marked sources to the right of the sensitivity line), suggesting they are reasonably well understood. There are a total of 93 sources in this group.

II. This class contains 12 H.E.S.S. sources whose behavior in the analysis seems contradicting as they are not expected to be seen with H.E.S.S., but still have been (marked red, located to the left of the sensitivity line).

III. The last category of sources contains the most interesting ones as these have not been detected with H.E.S.S. yet, but can theoretically be within a 30 h observation (marked blue, located to the right of the sensitivity line).There are 811 sources in this group but, as will be seen later, not all of these are prime candidates for follow-up observations.

The remaining 243 sources displayed in Figure 4.1, which are marked blue and located to the left of the sensitivity line, are not observable with H.E.S.S. within a 30 h observation and are therefore not investigated any further.
In the following sections each class of sources will be further analyzed and discussed.

4.2. Class I: Already observed Sources

The first class of sources contains 93 TeVCat objects, of which at least 77[5] were detected by the H.E.S.S. instrument. According to the analysis presented in the previous section this is no surprise as they are expected to be seen within a 30 h observation. This on one side already suggests that the sensitivity value calculated above (see Figure 4.1) is a good representation of the reality and on the other side that these sources are reasonably well understood.
As an example the Fermi and H.E.S.S. spectrum for HESS J1640-465 (or 3FHL J1640.6-4633) has been plotted in Figure 4.2. The very high energy (VHE, $E > 100\,\mathrm{GeV}$) γ-ray source was first discovered by H.E.S.S. in the Galactic Plane Survey (HGPS)[28] and is positionally coincident with the supernova remnant SNR G338.3-0-0. The X-ray pulsar PSR J1640-4631 has also been recently discovered [29] within the SNR shell. Fermi measured a spectral index of $\Gamma = 1.63 \pm 0.17$ for a simple power law while the H.E.S.S. data were fitted to an exponential power law with an index of $\Gamma = 2.11 \pm 0.19$ and a cutoff at $E_c = 6.0^{+2.0}_{-1.2}\,\mathrm{TeV}$ [30]. The fact that Fermi measured a harder spectral index is no surprise as high energy cutoffs, which are not unusual to be found in such objects, are not visible in its energy band (10 GeV-2 TeV). Nevertheless, the two flux points at higher energy of Fermi are (within their errors)

---

[5] 77 sources were detected by H.E.S.S. and published in scientific papers.

consistent with the H.E.S.S. spectrum. In addition to the spectra, the calculated pseudo-differential sensitivity (integral sensitivity for five bins of energy per decade) for 65 h of observations is, as expected, well below the measured flux points by H.E.S.S. (63.4 h of data).

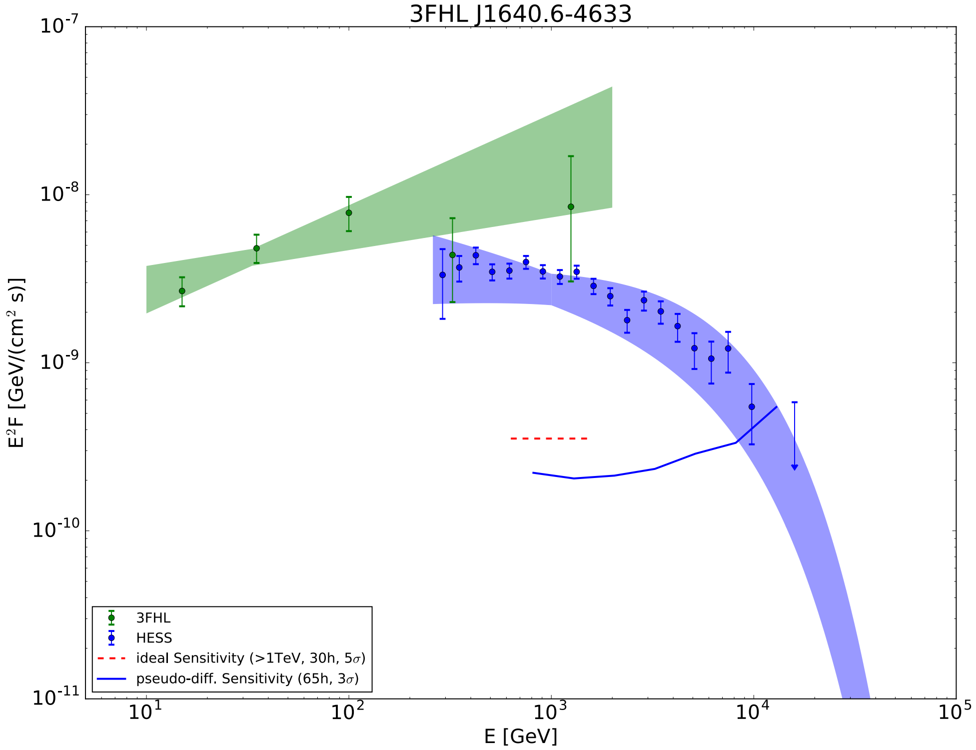

Figure 4.2.: γ-ray spectrum of HESS J1640-465 as measured by Fermi-LAT (green) and H.E.S.S. (blue) [30]. The blue line represents the pseudo-differential sensitivity (integral sensitivity for five bins of energy per decade). The live time of 65 h corresponds to the amount of data used to derive the H.E.S.S. spectrum. The dashed red line represents the ideal integral sensitivity above 1 TeV for a 30 h H.E.S.S. observation used in the initial analysis.

The remaining 16 sources in this class, which were not detected with H.E.S.S., were observed with other IACTs like MAGIC or VERITAS.

4.3. Class II: Sources with contradicting Results

Sources in this category are found in TeVCat and have been detected with H.E.S.S. although the analysis presented in Section 4.1 suggest that these can not be seen within a 30 h observation. There are a total of 12 such sources. The complete list can be found in Table 4.1. In this section a possible explanation shall be given on why these sources behave in such a way.

To determine if a source is observable or not, the analysis in Section 4.1 uses a combination of two factors: the extrapolated integral flux above 1 TeV based on the spectral information contained in the 3FHL catalog and the calculated integral sensitivity above 1 TeV for a 30 h observation under ideal conditions. Having already seen during the course of this thesis that the sensitivity tool produces sensible values, this leaves two possible explanations for the observed case: the spectral information stored in the 3FHL catalog for these sources is inaccurate or the sensitivity value is not representative for these sources as the used live time was too short.

3FHL Name	TeVCat Name	Γ_{3FHL}	Γ_{HESS}	t_{HESS} [h]
3FHL J1016.2-5857	TeV J1016-589	4.67 ± 1.82	2.9 ± 0.6	40
3FHL J1018.8-5857	TeV J1018-589	3.3 ± 0.4	2.2 ± 0.34	63.3
3FHL J1028.5-5818	TeV J1026-582	3.68 ± 0.55	1.94 ± 0.4	45.9
3FHL J1418.7-6058	TeV J1418-609	4.7 ± 0.9	2.22 ± 0.18	18.1
3FHL J1648.6-4610	TeV J1647-458	5.5 ± 1.4	2.19 ± 0.28	33.8
3FHL J1748.0-2446	TeV J1747-248	3.45 ± 0.69	2.5 ± 0.5	62
3FHL J1801.6-2327	TeV J1801-233	5.7 ± 1.3	2.66 ± 0.47	42
3FHL J1803.2-2147	TeV J1804-217	4.57 ± 0.59	2.72 ± 0.26	15.7
3FHL J1813.4-1245	TeV J1813-126	6.0 ± 1.6	-	-
3FHL J1826.1-1256	TeV J1826-130	3.91 ± 0.77	-	-
3FHL J1839.4-0553	TeV J1840-055	3.66 ± 0.82	2.41 ± 0.3	26
3FHL J1907.9+0602	TeV J1907+062	4.15 ± 0.75	2.1 ± 0.27	27

Table 4.1.: List of sources found during the analysis of the 3FHL catalog with contradicting results as they were deemed as "not observable" despite being already seen with H.E.S.S. and other instruments. Spectral information measured by H.E.S.S. were taken from [28, 31–39]

The latter argument does not seem to be particularly strong for several reasons: First, when examining the live times used to derive the H.E.S.S. spectra of the sources (see Table 4.1), it can be seen that there is no obvious pattern as there are cases for both exceeding and falling below the 30 h mark of the sensitivity value. While this suggest that for some cases the sensitivity value is indeed not completely representative, it does not fully explain the observed behavior. Referring back to Figure 4.1 is can be seen that the difference between the sensitivity (red line) and the extrapolated flux of the sources can be as big as three orders of magnitude. Calculating an improved sensitivity value by this amount would require absurdly high live times as $F \sim 1/\sqrt{t}$. The plotted spectra of the sources (see Figure 4.4 and Appendix A.3) also show the (pseudo-differential) sensitivity curve at 3σ with the respective live times of the H.E.S.S. spectrum. These confirm the above argumentation as the Fermi spectra are still orders of magnitude below the calculated sensitivities.
Seeing that the sensitivity value is not responsible for labeling these sources as "not observable" by H.E.S.S. even though they have been observed, this leaves only the sources' spectral information stored in the 3FHL catalog as a possible explanation. As already mentioned, the extrapolation of the flux of the 3FHL sources used to categorize them is dependent on

the accuracy of the spectral index measured by Fermi. The case of these sources is exactly where this extrapolation is not representative anymore. By comparing the spectral indices measured by Fermi and H.E.S.S. in Table 4.1 on can see that Fermi measured much softer spectra which means their flux at higher energies is much smaller. Normally one would expect or understand Fermi to measure harder spectral indices as it is possible that it will not see high energy cutoffs within its energy range that IACTs are able to pick up. Figure 4.3 shows a comparison of the spectral indices between associated sources in 3FHL and TeVCat, including the sources with contradicting analysis results. As can bee seen, there a basically two groups of objects. The first one shows the expected behavior and consists of sources where the Fermi index is harder (smaller) than the one in TeVCat (below the green line). The second one includes sources with a softer Fermi index (above the green line). The sources with contradicting results fall into this group and are displayed in red with their respective errors. They stand out in two ways: they are the softest Fermi sources in this group and the error on the Fermi index is huge. This means that the Fermi measurements regarding these sources is very inaccurate.

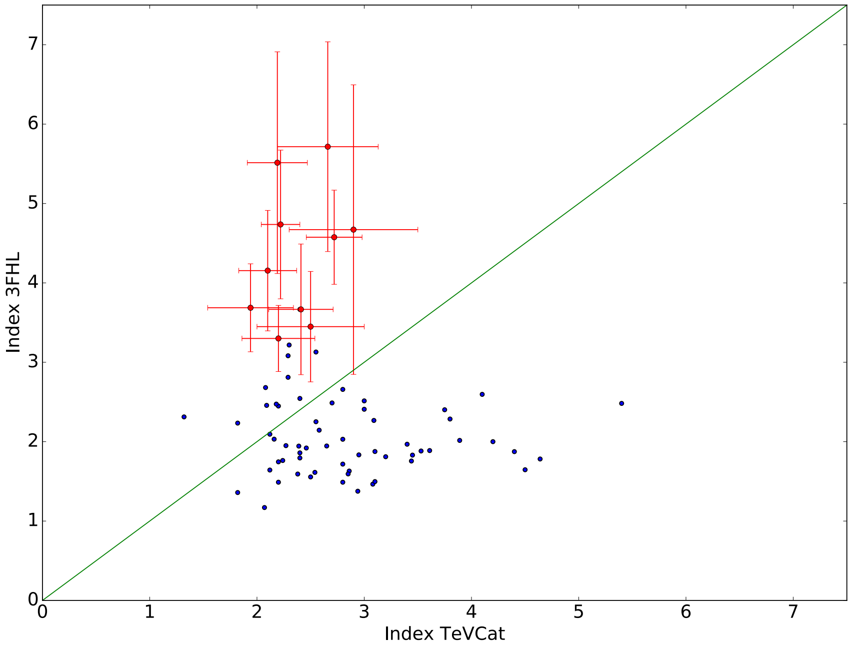

Figure 4.3.: Comparison between the spectral indices of associated sources in 3FHL and TeVCat. The red dots are shown with their respective errors and represent the class of sources with contradicting analysis results. The green linear line represents identical indices in both catalogs.

Figure 4.4 visualizes the measured spectra of Fermi and H.E.S.S. for two of these sources (the other spectra can be found in the Appendix A.3). Adding to the observations already discussed above, it is also noteworthy that the error on the flux points measured by Fermi, especially for the higher energies, is massive. Besides this, the plotted pseudo-differential sensitivities are in good agreement with the flux points measured by H.E.S.S., which verifies the sensitivity tool once again.

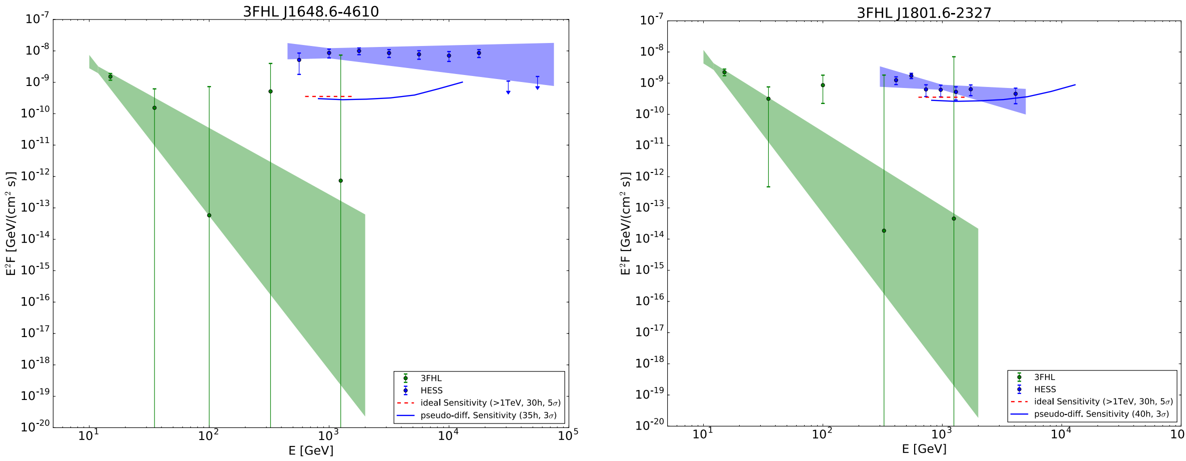

Figure 4.4.: γ-ray spectrum of TeV J1647-458 (**left**) and TeV J1801-233 (**right**) as measured by Fermi-LAT and H.E.S.S. The blue line represents the pseudo-differential sensitivity (integral sensitivity for five bins of energy per decade). The live times of 35 h and 40 h corresponds to the amount of data used to derive the H.E.S.S. spectra. The dashed red line displays the ideal integral sensitivity above 1 TeV for a 30 h H.E.S.S. observation used in the initial analysis.

In conclusion it can be said that the contradicting results of the analysis for these sources can most likely be explained by the inaccuracy of their Fermi data. These sources are among the softest when compared to their TeVCat counterparts and have unusually large errors on their spectral indices and flux points. Because of their soft index the extrapolation of their fluxes results in much lower values that ultimately lie below the calculated ideal sensitivity for H.E.S.S. and deems them as “not observable”.

4.4. Class III: Potential new Observation Canidates

This section focuses on the last and probably most interesting group of objects: the potential new observation candidates for H.E.S.S. The first analysis presented in Section 4.1 resulted in a total of 811 such candidates, though theses were only required to be geometrically observable from the H.E.S.S. site.

The next step is to reduce the amount of sources and filter out only the most promising ones. These are objects with constant emission, no visible cutoff up to 1 TeV and relatively hard spectra. Active sources are excluded because their variability makes them harder to observe and requires a well planned observation strategy that ensures a successful detection. As the analysis extrapolates the Fermi flux measured at 10 GeV up to 1 TeV for H.E.S.S. observations by using a simple power law, sources with cutoffs within this range lead to wrong results and are thus also avoided. Additionally, a relatively hard energy spectra is preferred as this ensures a high enough flux at higher energies. The most probable group of sources to fulfill these criteria are galactic sources.

To reduce the amount of candidates exactly the way intended a set of cuts is imposed (see Table 4.2). The first cut only allows sources to lie within ±10° of galactic latitude, i.e. in the galactic plane. This excludes most extragalactic objects. A second criteria removes all variable and any leftover extragalactic sources by cutting on the source type stored in the 3FHL catalog. The last cut limits the spectral index to be 3.0 at maximum and ensures a hard enough spectra for H.E.S.S. observations.

Parameter Name	Cut
GLAT	$-10^\circ < b < 10^\circ$
Class	*class* $\neq$ *bcu, bll, gal, bin, agn, sbg, fsrq*
Spectral Index	$\Gamma < 3.0$

Table 4.2.: List of applied cuts during the analysis of the sources from the 3FHL catalog

As a result a more manageable amount of 56 sources was obtained. A complete list can be found in Appendix A.4. Only seven of them show no cutoff or dip in the flux measurements by the Fermi-LAT between 10 GeV and 2 TeV. These are therefore the “prime” candidates for H.E.S.S. follow-up observations and will be investigated in detail in the following section while the remaining 49 sources will be discussed more briefly at the end of this chapter.

4.4.1. Prime Candidates

In this section the found “prime” candidates for follow-up H.E.S.S. observations are studied and discussed in more detail. This involves the calculation of sensitivities with the developed sensitivity tool as well as an analysis with the HAP software (done by M. Kraus and A. Ziegler).

Examining the parameters of the prime candidates as listed in Table 4.3 one can find a few noticeable things. First of all, their spectral indices lie between 1.7 and 2.6 and are therefore on the hard side. This is of course not surprising as soft sources were discarded during the analysis. While the analysis also only allows sources to be within 10° of galactic latitude b, four of the found objects are lying directly in the galactic plane with $|b| < 0.5^\circ$. Furthermore, six of sources are marked as “extended” in the 3FHL catalog. Three of them are classified as supernova remnants (SNR) which are often linked to extended γ-ray emission. Because of this it is unusual that the only point-like source among the candidates, 3FHL J1733.4-3942, is also labeled as SNR. A probable explanation could be that the source is actually linked to a neutron star or pulsar often found in the center of SNRs. The remaining three candidates have not been classified by Fermi.

Before beginning with the individual analysis for each source, first all available H.E.S.S. I data have been gathered. This was done with the help of a run selection script (*findruns.pl*) which searches the database for observation runs at the source position within a specified radius which was set to 2.0° with the additional criterion of at least three participating telescopes per run. Using this method a total amount of 225.59 h of data have been found for five of the seven candidates. The respective amount of data found for each source is listed in Table 4.3. Unfortunately 3FHL J1208.5-5243e and 3FHL J1733.4-3942 have no H.E.S.S. observation runs around their position which prevents them from being further analyzed.

3FHL Name	RA [°]	Dec [°]	l [°]	b [°]	Γ	Class	Live Time [h]
3FHL J0822.1-4253e	125.54	-42.89	260.31	-3.37	2.32	snr	18.76
3FHL J1036.3-5833e	159.09	-58.56	286.08	-0.18	1.74	-	67.56
3FHL J1112.1-6101e	168.04	-61.02	291.20	-0.43	2.25	-	56.86
3FHL J1208.5-5243e	182.13	-52.73	296.37	9.59	1.94	snr	-
3FHL J1213.3-6240e	183.35	-62.68	298.58	-0.13	2.55	snr	39.03
3FHL J1553.8-5325e	238.46	-53.43	328.13	0.28	2.13	-	43.38
3FHL J1733.4-3942	263.37	-39.70	349.54	-3.60	1.71	snr	-

Table 4.3.: List of prime candidates found during the analysis of the 3FHL catalog. The live times correspond to the amount of H.E.S.S. data found within a 2.0° search radius around the source position with at least three participating telescopes.

For each of the five remaining candidates a detailed analysis was performed. This involved the calculation of the achieved sensitivities with the available H.E.S.S. data, as well as running a HAP analysis ($\Theta^2 = 0.0125\,\mathrm{deg}^2$, *std zeta* cuts[6]) to obtain upper limits and a significance map. The results are presented in Figures 4.5, 4.6, 4.7, 4.8 and 4.9. The comparison between the spectra measured by Fermi and the calculated sensitivities initially would suggest that within the available live times all sources should have easily been seen by H.E.S.S. However, since the size of the ON-region used in the analysis is different from the extension of the sources (see Table 4.4) a correction needs to be applied on either side to obtain comparable results. It was chosen to correct the flux measurements from Fermi to match the analysis. The corrected flux is also displayed in the figures. Comparing it to the calculated sensitivity values reveals that 3FHL J1036.3-5833e is not expected to be seen with H.E.S.S. It features an unusually large extension of 2.465° (radius of the circular region) which is why the applied correction is dramatic. Such extended objects would realistically not be observable with H.E.S.S. anyway as its FoV has a radius of 2.5°. Based on the corrected flux at the higher energies (including errors) sources 3FHL J0822.1-4253e, 3FHL J1213.3-6240e and 3FHL J1553.8-5325e are marginal to detect within the H.E.S.S. data. Only the flux of 3FHL J1112.1-6101e lies above the sensitivity suggesting that this source could have already been seen.

The created significance maps partly contradict these conclusions as none shows any excess being detected at the target positions. The spots of higher significance (around 2σ) seen in some of the maps do not come from actual γ-events but are caused by background fluctuations. The significance map of 3FHL J1553.8-5325e shows the nearby source HESS J1552-530. However, an association between the 3FHL and H.E.S.S. source is unlikely as the spatial distance between the two is greater than the point spread function (PSF) of H.E.S.S.

---

[6] The gamma/hadron separation is based on TMVA when using std zeta cuts in HAP.

3FHL Name	Extension [°]
3FHL J0822.1-4253e	0.443
3FHL J1036.3-5833e	2.465
3FHL J1112.1-6101e	0.53
3FHL J1213.3-6240e	0.332
3FHL J1553.8-5325e	0.523

Table 4.4.: Size of the sources' extension. The values represent the radius of a circular region.

The source seen in the map for 3FHL J1112.1-6101e is a known source which had no exclusion region assigned to it. This however did not interfere with the analysis. The fact no signal whatsoever was detected is surprising (except for 3FHL J1036.3-5833e) and leads to the questions of possible reasons. The four sources are, as previously stated, all marked as "extended" with two being classified as SNRs. These are known to have pulsars at their center which often show cutoffs in their γ-ray spectra though they are typically not extended sources. It would be plausible for Fermi to not pick up such a cutoff in its measurements because of its lower operating range in terms of energy. This would mean that the real flux from the source is much lower at higher energies making it much harder for H.E.S.S. to observe the source. Such a "source confusion" is not unlikely as the population density of objects in the galactic plane is high. In this case it would however not explain why the emission Fermi measured is extended. Nonetheless, some sort of cutoff in the spectra still seems to be the most probable explanation. As the other two candidates, 3FHL J1112.1-6101e and 3FHL J1553.8-5325e, are not assigned by Fermi to any source type it is much harder to give a specific reason to why they do not show up in the data. But a likely reason is that they also feature a cutoff in their spectra at higher energies than Fermi could measure.

Besides the significance maps the HAP analysis was also used to derive upper limits for H.E.S.S. from the data using the Rolke method [40] (implemented in HAP). These are also shown in the respective figures for each source. Generally they are in good agreement with the calculated sensitivity curves which confirms the initial results. The small difference between the two curves is explainable by the fact that the upper limits are calculated based on a confidence level of 95 % ($\approx 2\sigma$) wheres the sensitivity curves are produced with a 5σ requirement. Furthermore, it is noteworthy that the obtained limits are in agreement with the corrected spectra from Fermi.

In conclusion, this part of the analysis showed that the data from Fermi and H.E.S.S. are, after correcting for the source extensions, mostly consistent with each other. Despite the calculated sensitivities suggested to see a signal from some of the source in the H.E.S.S. data, the significance maps showed no excess at all. However, there exist plausible scenarios such as cutoffs at higher energies, that could explain this behavior. Only the Fermi data for 3FHL J1036.3-5833e looks questionable as its extended region is unusually large. Therefore it seems appropriate to review the Fermi data on this position again.

With these result in mind, it is difficult to suggest a H.E.S.S. follow-up observation on any of these objects. The majority of sources already has live times $\gtrsim 40\,\mathrm{h}$ without being able to detect any signal. Hence, it is unlikely that new observations on these position will be able to reveal the associated H.E.S.S. counterparts to the Fermi sources anytime soon.

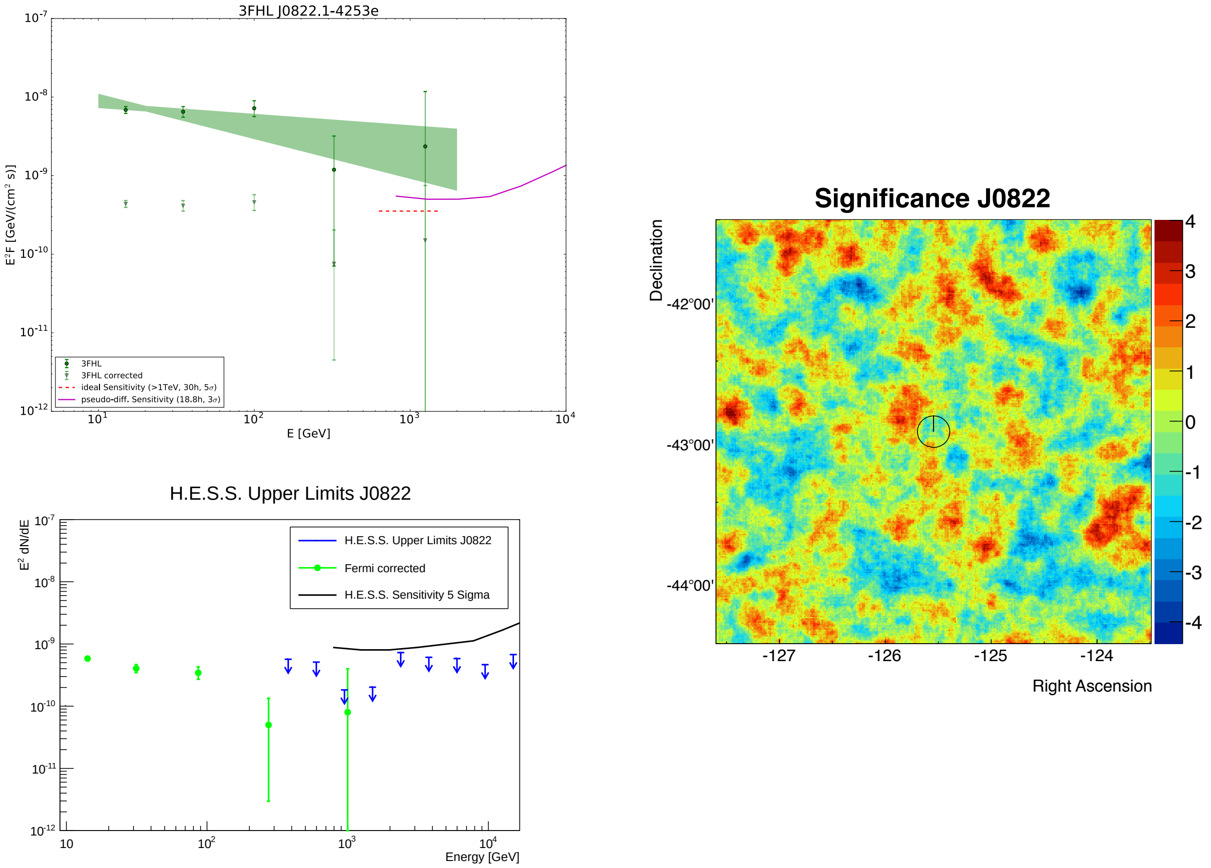

Figure 4.5.: Analysis results of 3FHL J0822.1-4253e: **Left top:** Flux and spectra as measured by the Fermi-LAT. The flux points have also been plotted with an applied correction that accounts for the different ON-region sizes of the sources and the sensitivity curve. The red-dashed line represents the integral sensitivity value > 1 TeV for a 30 h observation under ideal conditions used in the initial analysis. The magenta line displays the pseudo-differential sensitivity (integral sensitivity for five bins of energy per decade) calculated based on the available H.E.S.S. data (18.8 h). **Left bottom:** Calculated upper limits for H.E.S.S. in comparison with the pseudo-differential sensitivity. **Right:** Significance map based on the available H.E.S.S. data (Left bottom & right plot produced by M. Kraus)

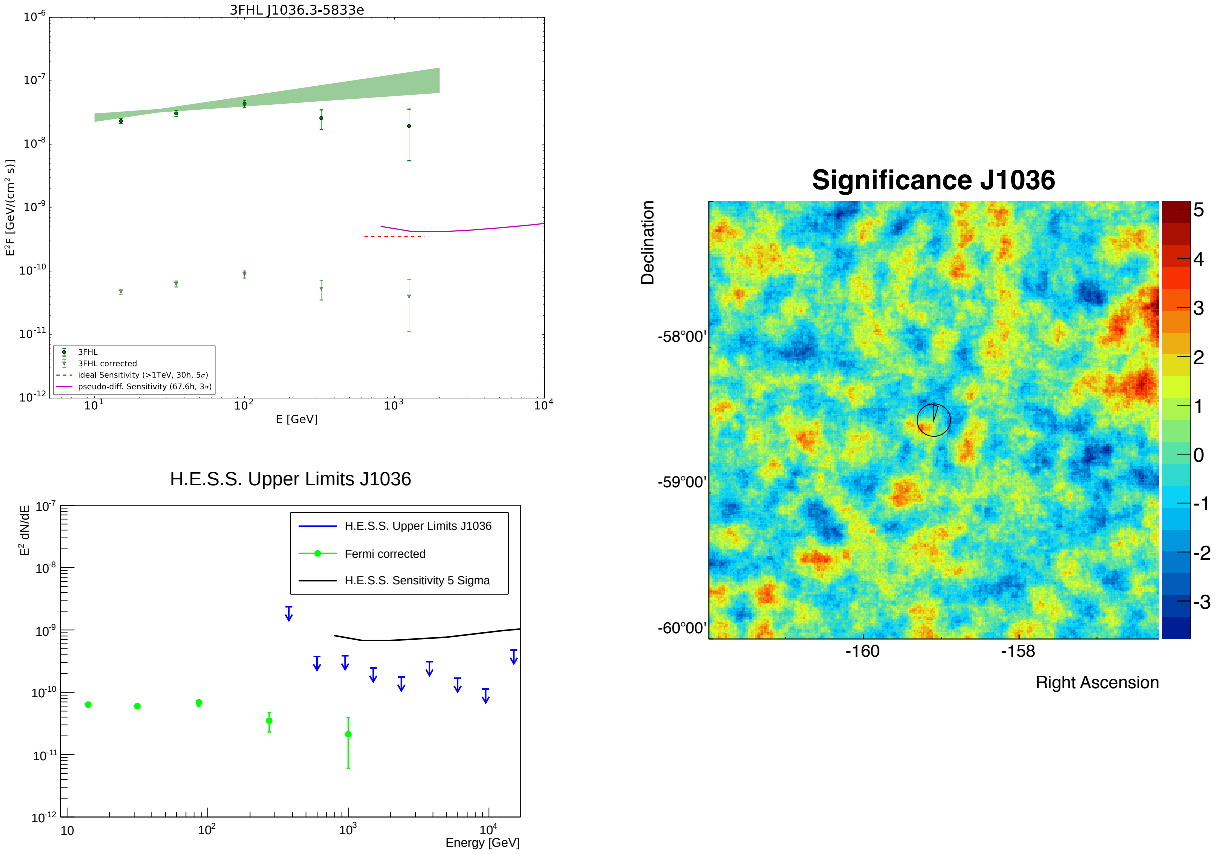

Figure 4.6.: Analysis results of 3FHL J1036.3-5833e: **Left top:** Flux and spectra as measured by the Fermi-LAT. The flux points have also been plotted with an applied correction that accounts for the different ON-region sizes of the sources and the sensitivity curve. The red-dashed line represents the integral sensitivity value > 1 TeV for a 30 h observation under ideal conditions used in the initial analysis. The magenta line displays the pseudo-differential sensitivity (integral sensitivity for five bins of energy per decade) calculated based on the available H.E.S.S. data (67.6 h). **Left bottom:** Calculated upper limits for H.E.S.S. in comparison with the pseudo-differential sensitivity. **Right:** Significance map based on the available H.E.S.S. data (Left bottom & right plot produced by M. Kraus)

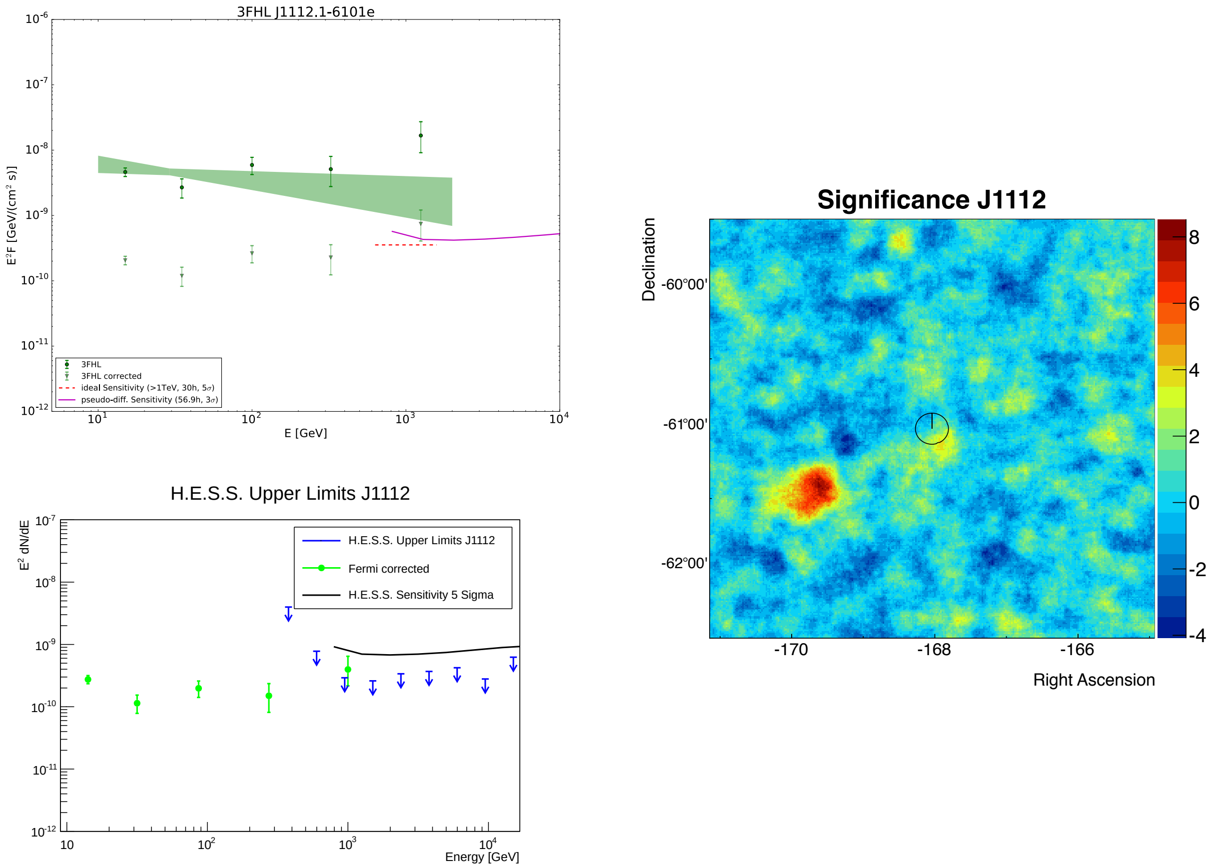

Figure 4.7.: Analysis results of 3FHL J1112.1-6101e: **Left top:** Flux and spectra as measured by the Fermi-LAT. The flux points have also been plotted with an applied correction that accounts for the different ON-region sizes of the sources and the sensitivity curve. The red-dashed line represents the integral sensitivity value > 1 TeV for a 30 h observation under ideal conditions used in the initial analysis. The magenta line displays the pseudo-differential sensitivity (integral sensitivity for five bins of energy per decade) calculated based on the available H.E.S.S. data (56.9 h). **Left bottom:** Calculated upper limits for H.E.S.S. in comparison with the pseudo-differential sensitivity. **Right:** Significance map based on the available H.E.S.S. data (Left bottom & right plot produced by M. Kraus)

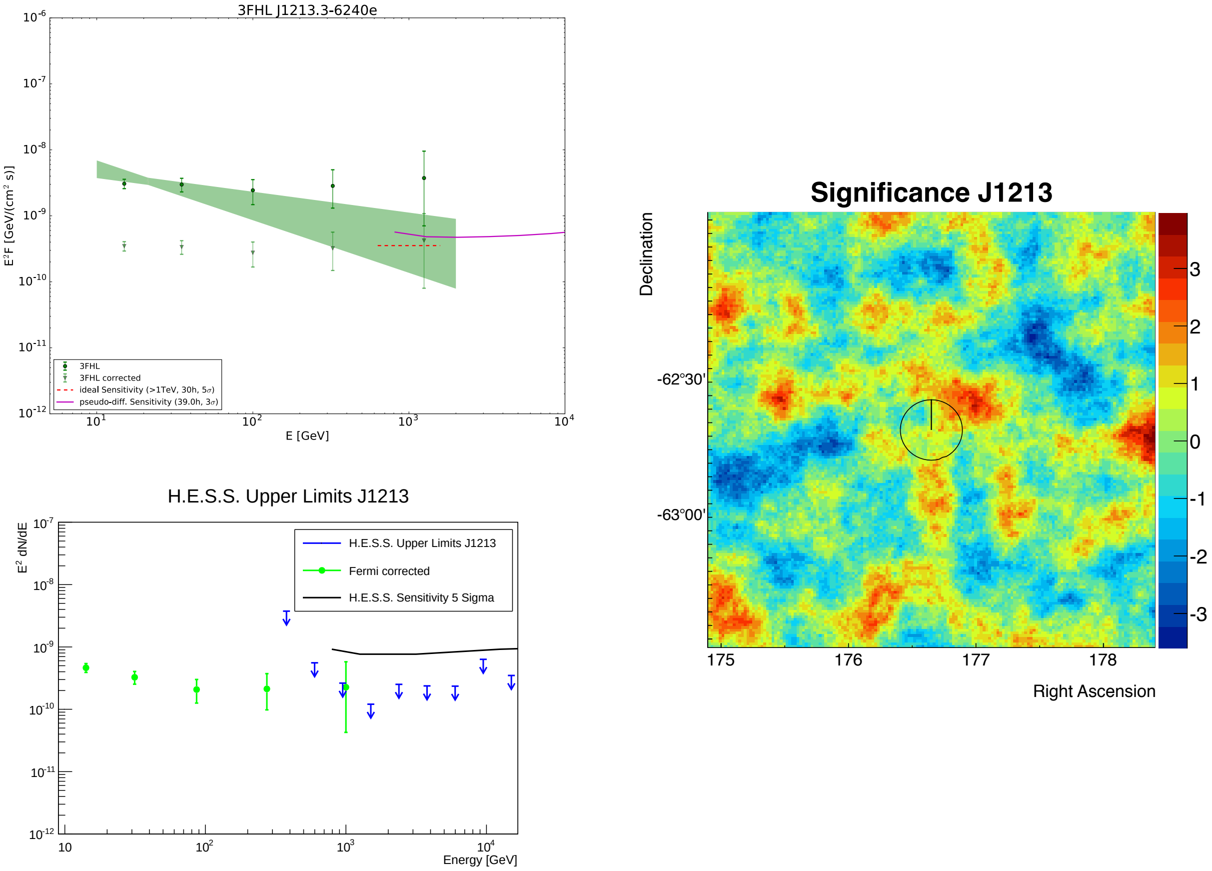

Figure 4.8.: Analysis results of 3FHL J1213.3-6240e: **Left top:** Flux and spectra as measured by the Fermi-LAT. The flux points have also been plotted with an applied correction that accounts for the different ON-region sizes of the sources and the sensitivity curve. The red-dashed line represents the integral sensitivity value $> 1\,\text{TeV}$ for a 30 h observation under ideal conditions used in the initial analysis. The magenta line displays the pseudo-differential sensitivity (integral sensitivity for five bins of energy per decade) calculated based on the available H.E.S.S. data (39.0 h). **Left bottom:** Calculated upper limits for H.E.S.S. in comparison with the pseudo-differential sensitivity. **Right:** Significance map based on the available H.E.S.S. data (Left bottom & right plot produced by M. Kraus)

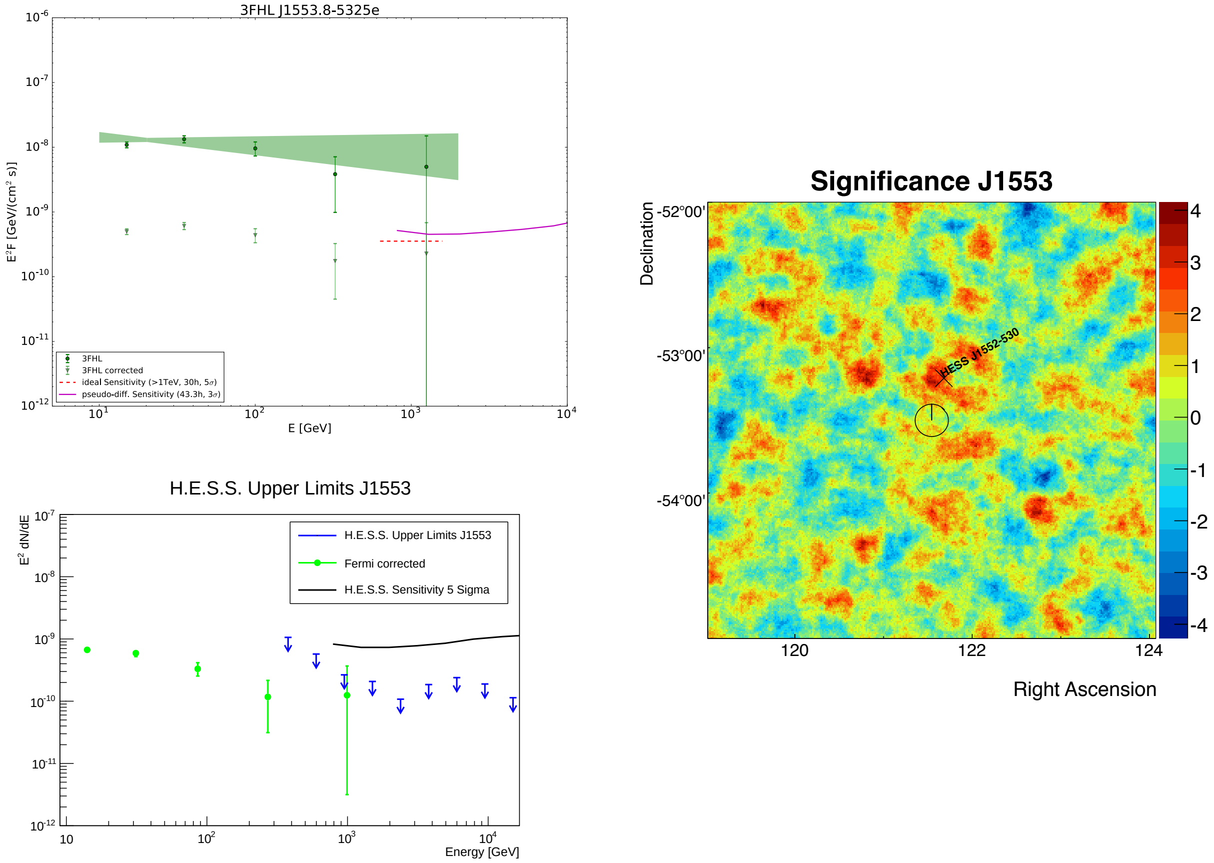

Figure 4.9.: Analysis results of 3FHL J1553.8-5325e: **Left top:** Flux and spectra as measured by the Fermi-LAT. The flux points have also been plotted with an applied correction that accounts for the different ON-region sizes of the sources and the sensitivity curve. The red-dashed line represents the integral sensitivity value > 1 TeV for a 30 h observation under ideal conditions used in the initial analysis. The magenta line displays the pseudo-differential sensitivity (integral sensitivity for five bins of energy per decade) calculated based on the available H.E.S.S. data (43.4 h). **Left bottom:** Calculated upper limits for H.E.S.S. in comparison with the pseudo-differential sensitivity. **Right:** Significance map based on the available H.E.S.S. data (Left bottom & right plot produced by M. Kraus)

4.4.2. Remaining Sources

At the beginning of Section 4.4 it was mentioned that a total of 56 potential sources for H.E.S.S. follow-up observations was found that fulfill the set criteria. The seven “prime” candidates that do not exhibit any cutoff or dip in the flux measurements done by Fermi were discussed in the previous section. However, the remaining 49 objects were also investigated (HAP analysis was done by M. Kraus and A. Ziegler). For 22 of them H.E.S.S. data in form of observation runs were found. The search criteria stayed the same: a search radius of 2.0° with the requirement of at least three participating telescopes per run. The individual amount of data for each source ranges from 0.4 h to 151.8 h. A detailed list of all sources can be found in the Appendix A.4. The outcome of the analysis shall be presented here in a brief fashion without the presentation of any additional plots.

Unfortunately, the results are very similar to the ones presented in the previous section. Despite some sources having well above 30 h of data, the created significance maps show no sign of notable excess for any of the source positions. The calculated upper limits for H.E.S.S. are in good agreement with the sensitivities obtained from the sensitivity tool as well as the spectra from the Fermi data. A probable scenario why these objectives have not been seen are cutoffs in the flux at higher energies.

Suggesting H.E.S.S. follow-up observation from this group of objects seems appropriate, as for some sources the amount of available H.E.S.S. data is < 15 h making it a reasonable assumption that adding more data could possibly reveal the H.E.S.S. counterpart for the 3FHL object. In order to pick out the best candidates the data will be further examined.

5. Conclusion and Outlook

At the start of this master thesis was the development of a sensitivity tool that provides a fast, easy and accurate way of calculating sensitivities for any position on the sky for the H.E.S.S. array. To achieve this task a technique for the estimation of γ- and background events needed to be constructed. While for the former a method was developed which uses the Crab nebula as a spectral template, the latter involved the implementation of a template background model combined with an accurate extraction method. In the end this task was successfully accomplished. The developed tool is able to calculate sensitivities based on either available H.E.S.S. data at the specified target position, or based on a list of specified parameters (e.g. expected zenith range, live times, camera offset).
The calculated sensitivities as well as the interim results have been verified in several ways. Cross-checks have been done with HAP analysis results based on runlists featuring different properties. This lead to the implementation of lower energy thresholds for the background model in order to be compatible. With these applied the sensitivities were in very good agreement with the ones derived from HAP up to energies of about 15 TeV. This was further confirmed later during the analysis of Fermi sources from the 3FHL catalog.
The final version of the sensitivity tool has some limitations. First of all, when calculating sensitivities based on H.E.S.S. data, only H.E.S.S. I runs with at least three participating telescopes are considered. This originates mainly from the used background model which is only valid under these circumstances. Furthermore, for the calculation of the sensitivities a simplified and practical formula is used (see Chapter 3.1). While this still provides good enough results and is often used for sensitivity calculations, a more accurate calculation can be achieved with the adaptation of Equation 17 from Li & Ma [22] which is usually used to claim discoveries. Therefore the next steps in improving the sensitivity tool should be the implementation of said formula as well as a modification of the existing or development of a new background model to extend the validity to H.E.S.S. II data.

With the functionality of the sensitivity tool verified, the second part of this thesis was the analysis of hard Fermi sources. The purpose was to find candidates for follow-up H.E.S.S. observations or see if some Fermi sources were already seen within the available data. The analysis was based on a pre-release version of the upcoming third catalog of Fermi high energy sources (10 GeV to 2 TeV), the 3FHL catalog. It contains a total of 1720 objects so the first step was to group these and select only the most interesting ones. As a criteria a nominal sensitivity value for the H.E.S.S. system for energies above 1 TeV assuming an observation time of 30 h was calculated with the sensitivity tool. By comparing this value to the extrapolated Fermi flux above 1 TeV of each source it was determined whether a source was observable or not. The found candidates were also checked for any TeVCat association.

Additionally, the analysis focused on galactic sources. In theory these provide the best candidates as they are more probable to have constant fluxes without a cutoff than extragalactic sources. Therefore a set of cuts on the parameters stored in the 3FHL catalog were applied (see Chapter 4.4).

During the analysis 12 sources were found that were deemed as "not observable" even though they had associations in the TeVCat meaning they were already detected by H.E.S.S. or another IACT. A deeper look into this matter revealed that it was caused by the combination of two factors: inaccurate spectral measurements from Fermi and the flux extrapolation used in the analysis. It turned out that the spectra measured by Fermi were much softer than their TeVCat counterparts. A comparison between the spectral indices of objects associated in 3FHL and TeVCat showed that this class of sources were among the softest on the Fermi side. As high energy cutoffs in the flux are often only detected by IACTs, it would be plausible for Fermi to measure harder spectra which is the behavior the other sources in the comparison showed. Because the analysis extrapolates the spectra from Fermi to the energy range most relevant for H.E.S.S. ($> 1\,\mathrm{TeV}$) using a simple power law, the softer Fermi spectra lead to a underestimation of the flux which is in turn what labeled these sources ultimately as "not observable". It was also noticed that the errors on the spectral indices as well as the flux points measured by Fermi were unusually large.

The analysis also found 56 potential candidates for H.E.S.S. follow-up observation. Seven sources were among the most promising, which were the ones with the highest and most constant flux over the Fermi energy range. These were labeled as "prime" candidates in this thesis. However, only for five of them H.E.S.S data was available. These were subsequently investigated in more detail. All candidates were labeled as "extended" in the 3FHL catalog and classified as either supernova remnants (SNRs) or had no classification. At first the already achieved sensitives with the available H.E.S.S. data were calculated. Comparing these to the flux measurements by Fermi, which were corrected because of the sources' extensions, revealed that one source is after all not expected to be observed (3FHL J1036.3-5833e), the detection of three is marginal within the errors (3FHL J0822.1-4253e, 3FHL J1213.3-6240e and 3FHL J1553.8-5325e) and only one is expected to be seen in the H.E.S.S. data (3FHL J1112.1-6101e). Following this, a HAP analysis on the sources was performed (by M. Kraus and A. Ziegler) to derive significance maps. Surprisingly, no excess whatsoever was visible in any of the maps at the target positions. One possible reason could be that these sources feature cutoffs in their fluxes at higher energies. Besides the significance maps the HAP analysis was also used to calculate upper limits for H.E.S.S. These were in good agreement with the calculated sensitivities as well as the Fermi spectra.

Suggesting follow-up observations to any of the investigated sources seems inappropriate. Because none of them showed any excess in the significant maps and most of them have already $\gtrsim 40\,\mathrm{h}$ of available data, it is unlikely that new observations will reveal the H.E.S.S. counterpart for the Fermi sources. Besides, it is suggested to redo a Fermi analysis on the source 3FHL J1036.3-5833e. It features an unusually large extension of 2.456° (radius of a circular region) which was the reason it was not expected to be seen with H.E.S.S. after applying the appropriate flux corrections.

Apart from the "prime" candidates the other remaining sources were also investigated by performing a HAP analysis. This work was mainly done by M. Klaus and A. Ziegler but some of the results have also been discussed in this work. For 22 of the remaining sources H.E.S.S. data were available. The results from this analysis were very similar to the previous ones. None of the sources showed any significant excess at the source positions suggesting they might feature a cutoff in their spectra. The calculated upper limits were also in good agreement with the Fermi spectra as well as with the calculated sensitivities. As some of these sources have less than 15 h of available data, follow-up observations might make sense. To determine this, these candidates will be examined further. In addition the sources which have no available H.E.S.S. data are also worth looking into. The sensitivity tool would be able to estimate the expected sensitivities for these objects.

Another possibility to find candidates for follow-up H.E.S.S. observation, which was not investigated during this master thesis, is to include extragalactic objects in the search. The coverage outside of the galactic plane by H.E.S.S. is relatively slim meaning the probability to find new H.E.S.S. sources might be higher. It is however not uncommon for these sources to have cutoffs or variable emission. Therefore, observations are more complicated to suggest as they require a more sophisticated strategy to ensure a detection.

A. Appendix

A.1. Calculating Ideal Sensitivities

The term “ideal” sensitivity in this thesis refers to sensitivities calculated for nearly optimal but not unrealistic observation conditions. They were also calculated with the sensitivity tool, albeit with a modified version of it. Instead of using a runlist as input and extracting certain run parameters form it, the required parameters were hard coded in the tool. The list of parameters with the used values can be found in Table A.1. The basic calculations in the tool remain the same and are explained in detail in Chapter 3.

Parameter	Value
Altitude	80 - 90° (Bin 12)
Azimuth	0 and 180°
Camera offset	0.5°
Muon phase	200
Telescope pattern	30
ON-region size	$0.0125\,\mathrm{deg}^2$
Live time	*various*
Significance	3 or $5\,\sigma$

Table A.1.: Parameter values used to calculate ideal sensitivities.

While for the background calculation the absolute value for the offset position in the camera was set at 0.5°, during the calculation the average of four different offset positions was used. In detector coordinates these positions are $(0.0, \pm 0.5)^\circ$ and $(\pm 0.5, 0.0)^\circ$. Similarly, the average between 0° and 180° of azimuth was applied during the background calculation, as well as for the creation for effective area histograms.

By modifying the parameter values found in Table A.1 this version of the tool is also capable of calculating sensitivities for sources where no H.E.S.S. observation runs can be found.

A.2. Additional Information concerning the Verification Steps

The verification of the background and sensitivities presented in Chapter 3.2.3 and 3.3 were done based on “mixed” runlists covering a wider altitude range and containing a sufficient amount of data. This section describes the runlists in detail and displays the plots which were not already shown in the chapters.

A.2.1. The “mixed” Runlists

The runlists and their properties used to verify calculated background and sensitivities by the tool are listed in the following table.

ID	Source	Runs	total Live Time [h]	Altitude range [°]	Azimuth [°]
a	Crab nebula	30	12.51	32.5 - 47.5	0
b	Crab nebula	39	16.02	37.5 - 47.5	0
c	PKS 2155-304	40	17.45	47.5 - 65.0	180
d	PKS 2155-304	50	21.55	47.5 - 80.0	180
e	PKS 2155-304	50	22.23	42.5 - 80.0	180

Table A.2.: Runlists used to verify the calculated background and sensitivities.

A.2.2. Additional Background Verification Plots

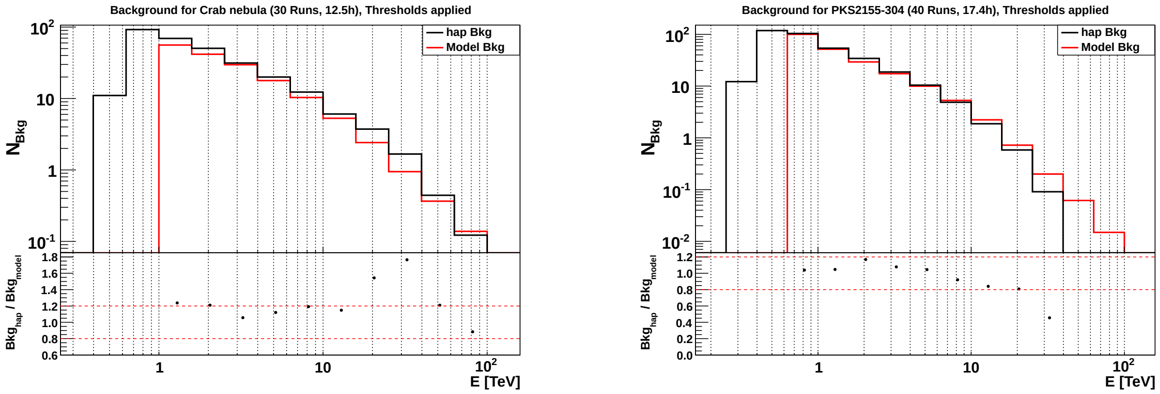

Runlist a

Runlist c

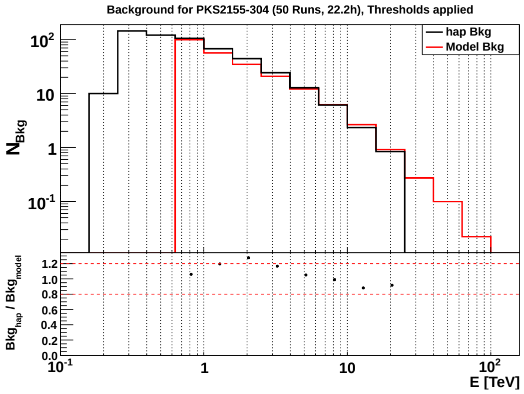

Runlist e

Figure A.1.: Comparison between the calculated background events from the model and HAP-analysis (*std*-cuts) for the shown runlists.

A.2.3. Additional Sensitivity Verification Plots

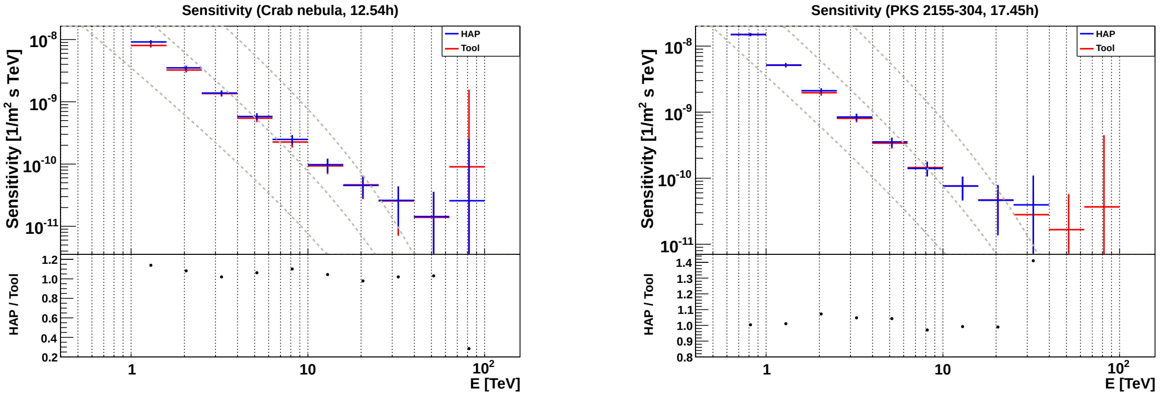

Runlist a

Runlist c

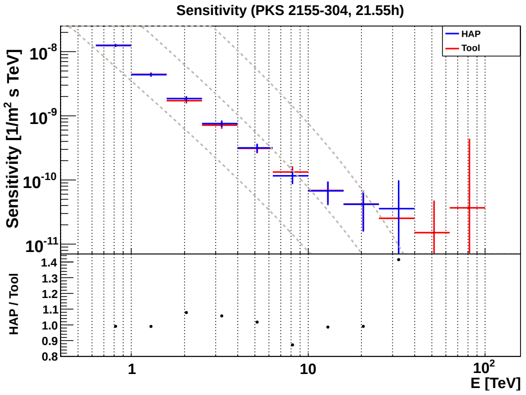

Runlist d

Figure A.2.: Pseudo-differential sensitivities (integral sensitivities for five bins of energy per decade) for the shown runlists. The sensitivities calculated from the tool are compared to the ones derived from the HAP analysis. The dotted grey lines represent 1 %, 10 % and 100 % of the Crab nebula flux.

A.3. Additional Spectra for the Sources with contradicting Results (Class II)

This chapter contains additional plots for the group of sources with contradicting analysis results. They were deemed as “not observable” but still have been seen with H.E.S.S. or other instruments. The plots display the spectra measured by Fermi and H.E.S.S.

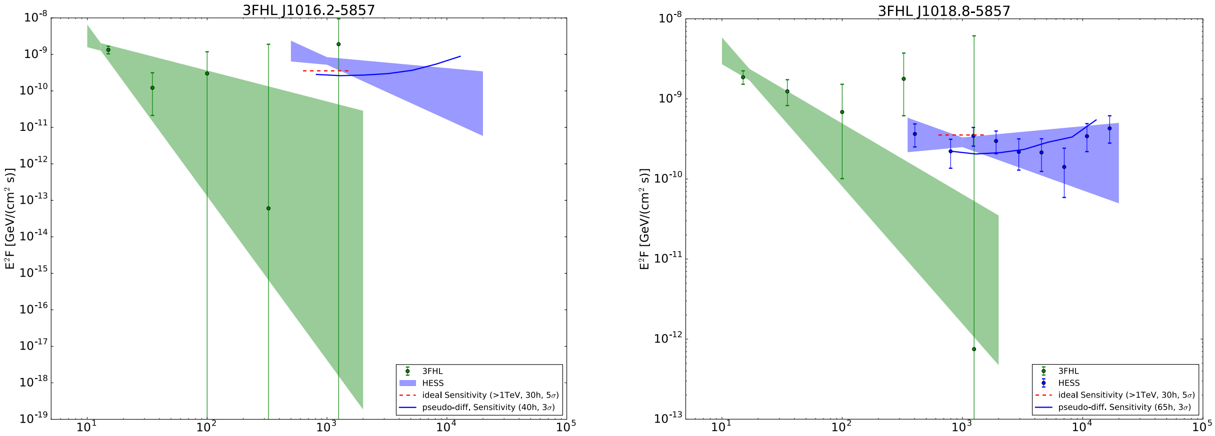

TeV J1016-589 TeV J1018-589

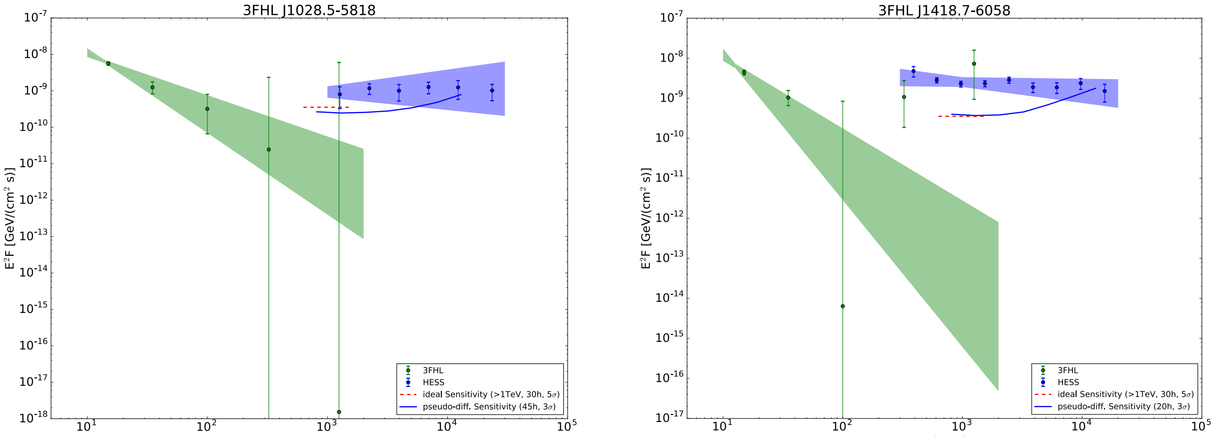

TeV J1026-582 TeV J1418-609

Figure A.3.: (1) Additional γ-ray spectra for the group of sources with contradicting analysis results as measured by Fermi-LAT (green) and H.E.S.S. The blue line represents the pseudo-differential sensitivity (integral sensitivity for five bins of energy per decade). Their live times corresponds to the amount of data used to derive the H.E.S.S. spectra. The dashed red line represents the ideal integral sensitivity above 1 TeV for a 30 h H.E.S.S. observation used in the initial analysis.

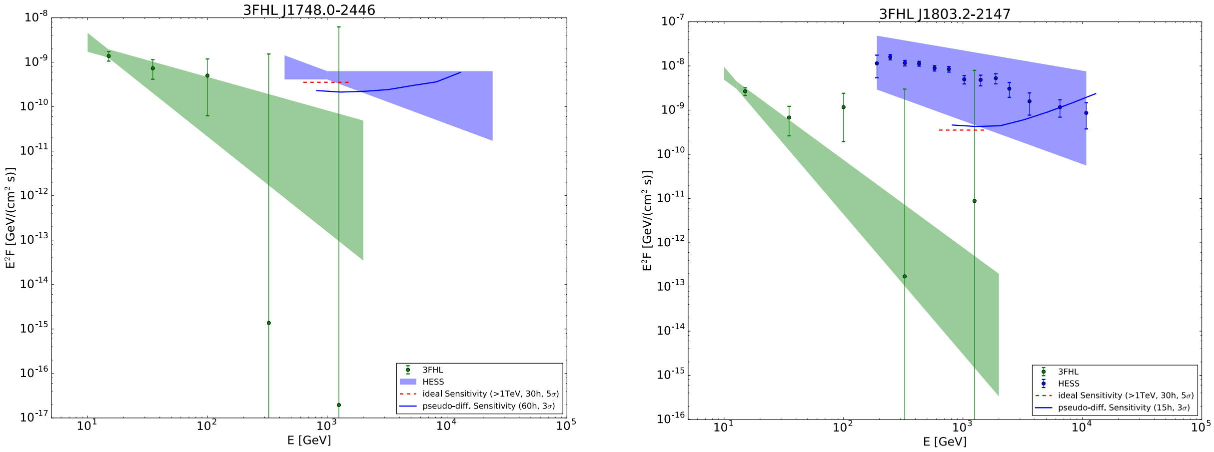

TeV J1747-248

TeV J1804-217

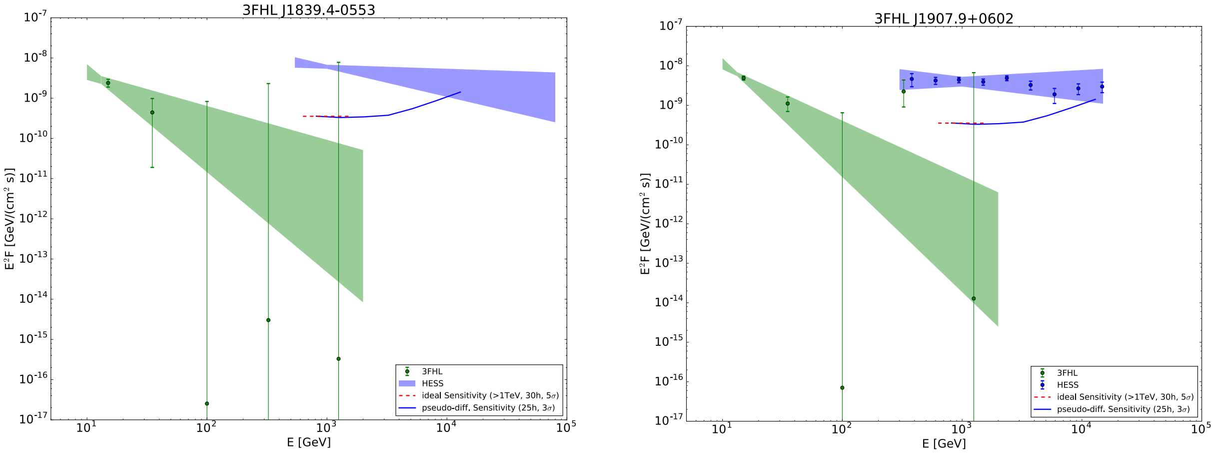

TeV J1840-055

TeV J107+062

Figure A.4.: (2) Additional γ-ray spectra for the group of sources with contradicting analysis results as measured by Fermi-LAT (green) and H.E.S.S. The blue line represents the pseudo-differential sensitivity (integral sensitivity for five bins of energy per decade). Their live times corresponds to the amount of data used to derive the H.E.S.S. spectra. The dashed red line represents the ideal integral sensitivity above 1 TeV for a 30 h H.E.S.S. observation used in the initial analysis.

A.4. Potential new Sources (Class III)

Below is a list of all potential sources found during the analysis with the applied cuts as listed in Chapter 4.4.

3FHL Name	RA [°]	Dec [°]	l [°]	b [°]	Γ	Live Time [h]
3FHL J0538.7+1643	84.68	16.72	189.61	-7.74	1.69	-
3FHL J0600.3+1245	90.09	12.76	195.71	-5.23	2.02	-
3FHL J0706.1+0248	106.54	2.80	212.11	4.55	1.21	-
3FHL J0709.7-3008	107.44	-30.14	241.96	-9.64	2.20	2.15
3FHL J0725.4+0217	111.37	2.29	214.77	8.62	2.44	-
3FHL J0725.7-0548	111.43	-5.81	222.05	4.92	1.96	-
3FHL J0752.4-1633	118.11	-16.56	234.67	5.42	1.76	-
3FHL J0820.2-2802	125.06	-28.05	247.86	4.72	1.35	-
3FHL J0822.1-4253e	125.54	-42.89	260.31	-3.37	2.32	18.76
3FHL J0852.5-3124	133.14	-31.40	254.77	8.36	1.85	-
3FHL J0928.5-5256	142.14	-52.93	275.11	-1.39	1.66	12.86
3FHL J1033.4-5033	158.36	-50.56	281.70	6.53	2.68	-
3FHL J1036.3-5833e	159.09	-58.56	286.08	-0.18	1.74	67.56
3FHL J1048.4-5030	162.10	-50.51	283.77	7.72	1.10	-
3FHL J1101.4-6049	165.35	-60.83	289.92	-0.76	1.95	31.35
3FHL J1112.1-6101e	168.04	-61.02	291.20	-0.43	2.25	56.86
3FHL J1115.0-6118	168.76	-61.31	291.62	-0.57	1.46	58.97
3FHL J1117.2-5338	169.31	-53.63	289.13	6.69	2.89	-
3FHL J1124.4-5916	171.10	-59.27	292.01	1.74	2.38	42.83
3FHL J1125.0-5806	171.27	-58.11	291.71	2.86	1.62	15.81
3FHL J1208.5-5243e	182.13	-52.73	296.37	9.59	1.94	-
3FHL J1213.3-6240e	183.35	-62.68	298.58	-0.13	2.55	39.03
3FHL J1240.5-7148	190.15	-71.81	302.07	-8.96	2.47	-
3FHL J1305.5-6240	196.39	-62.68	304.55	0.14	2.13	151.77
3FHL J1346.2-6026	206.56	-60.44	309.65	1.72	2.87	18.87
3FHL J1405.1-6118	211.28	-61.30	311.66	0.31	2.42	28.13
3FHL J1409.1-6121e	212.29	-61.35	312.11	0.12	2.24	-
3FHL J1526.3-4501	231.59	-45.03	329.58	9.68	1.77	-
3FHL J1528.4-6730	232.12	-67.51	317.12	-9.07	1.78	-
3FHL J1534.0-5231	233.50	-52.53	326.31	2.80	2.70	6.99
3FHL J1536.3-4949	234.09	-49.83	328.19	4.78	2.98	-
3FHL J1544.9-6641	236.25	-66.69	318.92	-9.37	1.96	-

3FHL Name	RA [°]	Dec [°]	l [°]	b [°]	Γ	Live Time [h]
3FHL J1547.9-5132	236.98	-51.54	328.61	2.30	2.83	19.22
3FHL J1552.7-5611e	238.20	-56.19	326.26	-1.76	2.34	36.40
3FHL J1553.8-5325e	238.46	-53.43	328.13	0.28	2.13	43.38
3FHL J1604.6-4441	241.16	-44.69	335.17	5.75	2.11	-
3FHL J1619.8-6315	244.96	-63.26	324.02	-9.28	2.32	-
3FHL J1655.5-4737e	253.88	-47.63	339.10	-2.65	1.77	28.85
3FHL J1657.5-4654	254.39	-46.91	339.88	-2.48	2.98	31.07
3FHL J1719.0-5348	259.76	-53.81	336.33	-9.31	1.70	-
3FHL J1729.9-4148	262.50	-41.80	347.42	-4.19	2.48	-
3FHL J1733.4-3942	263.37	-39.70	349.54	-3.60	1.71	-
3FHL J1733.8-4734	263.46	-47.57	342.91	-7.88	1.92	-
3FHL J1744.5-2609	266.13	-26.16	2.24	1.65	2.25	58.29
3FHL J1748.1-1944	267.04	-19.73	8.18	4.27	1.92	0.44
3FHL J1748.5-0854	267.15	-8.90	17.65	9.64	1.42	-
3FHL J1754.2-4334	268.56	-43.57	348.22	-8.92	2.84	-
3FHL J1811.2-2800	272.80	-28.00	3.62	-4.41	2.32	3.77
3FHL J1855.3+0751	283.83	7.86	40.38	2.72	1.64	7.08
3FHL J1856.1-1221	284.03	-12.35	22.41	-6.62	2.02	-
3FHL J1911.5+0310	287.89	3.17	38.06	-3.02	2.88	13.57
3FHL J1911.7+1448	287.95	14.80	48.40	2.30	1.85	5.31
3FHL J1917.9+0331	289.50	3.52	39.11	-4.28	1.60	10.53
3FHL J1927.5+0153	291.88	1.89	38.77	-7.15	1.59	-
3FHL J1949.5+0906	297.40	9.11	47.81	-8.53	2.14	-
3FHL J1958.1+2437	299.53	24.63	62.29	-2.41	1.42	12.25

Table A.3.: All found potential sources for H.E.S.S. during the analysis in Chapter 4.4 with the listed cuts. The source data are taken from the 3FHL catalog. The live times correspond to the amount of H.E.S.S. data (observations runs) found within a 2.0° search radius around the source position with at least three participating telescopes.

Bibliography

[1] NASA/DOE/Fermi LAT Collaboration. `http://fermi.gsfc.nasa.gov/ssc/observations/types/allsky/`. [Online; accessed 03-December-2016]. 1.1, A.4

[2] Mathieu de Naurois. The Very High Energy Sky from 20 GeV to Hundreds of TeV - Selected Highlights. *PoS*, ICRC2015:021, 2016. 1.1, A.4

[3] V. F. Hess. Über Beobachtungen der durchdringenden Strahlung bei sieben Freiballonfahrten. *Z. Phys.*, 13:1084, 1912. 2.1

[4] W. Bietenholz. The most powerful particles in the Universe: a cosmic smash. 2013. 2.1, A.4

[5] A. A. Abdo et. al. Observation of supernova remnant ic 443 with the fermi large area telescope. *The Astrophysical Journal*, 712(1):459, 2010. 2.1.1

[6] M. Cardillo, M. Tavani, A. Giuliani, S. Yoshiike, H. Sano, T. Fukuda, Y. Fukui, G. Castelletti, and G. Dubner. The Supernova Remnant W44: confirmations and challenges for cosmic-ray acceleration. *Astron. Astrophys.*, 565:A74, 2014.

[7] A. A. Abdo et al. Fermi-LAT Discovery of Extended Gamma-ray Emission in the Direction of Supernova Remnant W51C. *Astrophys. J.*, 706:L1–L6, 2009.

[8] H. Abdalla et al. The supernova remnant W49B as seen with H.E.S.S. and Fermi-LAT. 2016. 2.1.1

[9] A. Abramowski et al. Acceleration of petaelectronvolt protons in the Galactic Centre. *Nature*, 531:476, 2016. 2.1.1

[10] S. Funk. *A new population of very high-energy γ-ray sources detected with H.E.S.S. in the inner part of the Milky Way*. PhD thesis, Ruprecht-Karls-Universität Heidelberg, 2005. 2.1.1, 2.2.2

[11] S. Funk. Space- and Ground-Based Gamma-Ray Astrophysics. 2015. 2.1.2, 2.2, 2.3, 2.4, 3.1, A.4

[12] J. A. Hinton and W. Hofmann. Teraelectronvolt astronomy. *Ann. Rev. Astron. Astrophys.*, 47:523–565, 2009. 2.1.2, 2.11, A.4

[13] Z. Deretsky. National Science Foundation. `http://www.zina-studio.com/p489212137/ef1b5103`. [Online; accessed 20-August-2016]. 2.5, A.4

[14] K. Bernlohr. Simulation of Imaging Atmospheric Cherenkov Telescopes with CORSIKA and sim_telarray. *Astropart. Phys.*, 30:149–158, 2008. 2.6, A.4

[15] Walter Heitler. *The Quantum Theory of Radiation; 3rd ed.* International series of monographs on physics. Clarendon Press, Oxford, 1954. 2.2.1

[16] J. Matthews. A Heitler model of extensive air showers. *Astropart. Phys.*, 22:387–397, 2005. 2.7, A.4

[17] M. de Naurois and D. Mazin. Ground-based detectors in very-high-energy gamma-ray astronomy. *Comptes Rendus Physique*, 16:610–627, 2015. 2.2.1, 2.2.1, 2.2.1, 2.2.1, 2.9, A.4

[18] A. Haungs et al. KCDC - The KASCADE Cosmic-ray Data Centre. *J. Phys. Conf. Ser.*, 632(1):012011, 2015. 2.8, A.4

[19] K. Bernlöhr. Max-Planck-Institut für Kernphysik (MPIK), Heidelberg. `https://www.mpi-hd.mpg.de/hfm/CosmicRay/ChLight/ChLat`. [Online; accessed 22-August-2016]. 2.10, A.4

[20] J. Holder. Atmospheric Cherenkov Gamma-ray Telescopes. 2015. 2.2.3, 2.12, A.4

[21] Clementina Medina. H.E.S.S. Collaboration. `https://www.mpi-hd.mpg.de/hfm/HESS/pages/press/2012/HESS_II_first_light`. [Online; accessed 24-August-2016]. 2.13, A.4

[22] T. P. Li and Y. Q. Ma. Analysis methods for results in gamma-ray astronomy. *Astrophys. J.*, 272:317–324, 1983. 3.1, 5

[23] F. Aharonian et al. Observations of the Crab Nebula with H.E.S.S. *Astron. Astrophys.*, 457:899–915, 2006. 3.2.2, 3.3

[24] Michael Mayer. Background modelling for ctools. `https://hess-confluence.desy.de/confluence/display/HESS/Background+Modelling+for+ctools`. [Online; internal site; accessed 30-October-2016]. 3.2.3

[25] David Berge, S. Funk, and J. Hinton. Background Modelling in Very-High-Energy gamma-ray Astronomy. *Astron. Astrophys.*, 466:1219–1229, 2007. 3.2.3, 3.5, A.4

[26] A. Abramowski et al. Discovery of variable VHE γ-ray emission from the binary system 1FGL J1018.6–5856. *Astron. Astrophys.*, 577:A131, 2015. 3.3

[27] Scott Wakely and Deirdre Horan. TeVCat. `http://tevcat.uchicago.edu`. [Online; accessed 01-December-2016]. 4

[28] F. Aharonian et al. The H.E.S.S. survey of the inner galaxy in very high-energy gamma-rays. *Astrophys. J.*, 636:777–797, 2006. 4.2, 4.1

[29] E. V. Gotthelf et al. NuSTAR Discovery of a Young, Energetic Pulsar Associated with the Luminous Gamma-ray Source HESS J1640-465. *Astrophys. J.*, 788:155, 2014. 4.2

[30] A. Abramowski et al. HESS J1640-465 - an exceptionally luminous TeV γ-ray supernova remnant. *Mon. Not. Roy. Astron. Soc.*, 439(3):2828–2836, 2014. 4.2, 4.2, A.4

[31] A. Abramowski et al. Discovery of VHE emission towards the Carina arm region with the H.E.S.S. telescope array: HESS J1018-589. *Astron. Astrophys.*, 541:A5, 2012. 4.1

[32] A. Abramowski et al. Discovery of variable VHE γ-ray emission from the binary system 1FGL J1018.6–5856. *Astron. Astrophys.*, 577:A131, 2015.

[33] A. Abramowski et al. Revisiting the Westerlund 2 Field with the H.E.S.S. Telescope Array. *Astron. Astrophys.*, 525:A46, 2011.

[34] F. Aharonian et al. Discovery of the two wings of the Kookaburra complex in VHE gamma -rays with H.E.S.S. *Astron. Astrophys.*, 456:245, 2006.

[35] A. Abramowski et al. Discovery of extended VHE γ-ray emission from the vicinity of the young massive stellar cluster Westerlund 1. *Astron. Astrophys.*, 537:A114, 2012.

[36] A. Abramowski et al. Very-high-energy gamma-ray emission from the direction of the Galactic globular cluster Terzan 5. *Astron. Astrophys.*, 531:L18, 2011.

[37] F Aharonian. Discovery of very high energy gamma-ray emission coincident with molecular clouds in the W28 (G6.4-0.1) field. *Astron. Astrophys.*, 481:401, 2008.

[38] F. Aharonian. HESS VHE Gamma-Ray Sources Without Identified Counterparts. *Astron. Astrophys.*, 477:353–363, 2008.

[39] F. Aharonian. Detection of Very High Energy radiation from HESS J1908+063 confirms the Milagro unidentified source MGRO J1908+06. *Astron. Astrophys.*, 499:723, 2009. 4.1

[40] Wolfgang A. Rolke, Angel M. Lopez, and Jan Conrad. Limits and confidence intervals in the presence of nuisance parameters. *Nucl. Instrum. Meth.*, A551:493–503, 2005. 4.4.1

List of Figures

Danksagung

An dieser Stelle möchte ich mich bei allen Personen bedanken, die mich bei der Erstellung dieser Masterarbeit unterstüzt haben. Besonders bedanken möchte ich mich bei:

- **Prof. Dr. Stefan Funk** für die Vergabe dieses interessanten Themas, für die vielen hilfreichen Diskussionen und Anregungen und die Betreuung dieser Mastererbeit.
- **Prof. Dr. Christopher van Eldik** für die Übernahme des Zweitgutachtens.
- **Dr. Tobias Jogler** für die sehr gute Betreuung während der Arbeit.
- **Alexander Ziegler** für das Beantworten meiner vielen Fragen, der Hilfestellung beim Background Modell und dem Bereitstellen der HAP-Analyse Ergebnisse für die 3FHL Quellen.
- **Manuel Kraus** ebenfalls für die Bereitstellung der HAP-Analyse Ergebnisse der 3FHL Quellen, als auch für das Korrekturlesen meiner Arbeit.
- **Dr. Lars Mohrmann** für das Korrekturlesen meiner Arbeit.
- **Christopher Schönwälder** für die schöne Zeit im gemeinsamen Büro, die vielen spannenden Diskussionen und lustigen Gespräche.
- meiner Mutter, **Adelgunde Holzmeier**, und meiner Großmutter, **Katharina Kreutzer**, ohne deren Unterstützung weder mein Studium noch diese Arbeit in dieser Form möglich gewesen wären.

Erklärung

Ich versichere, dass ich meine Masterarbeit ohne Hilfe Dritter und ohne Benutzung anderer als der angegebenen Quellen und Hilfsmittel angefertigt habe und die aus benutzten Quellen wörtlich oder inhaltlich entnommenen Stellen als solche kenntlich gemacht habe. Diese Arbeit hat in gleicher oder ähnlicher Form noch keiner Prüfungsbehörde vorgelegen.

Nürnberg, den 19. Dezember 2016

Jens Holzmeier